Mechanical Systems and Signal Processing 200 (2023) 110587

Contents lists available at ScienceDirect

Mechanical Systems and Signal Processing

journal homepage: www.elsevier.com/locate/ymssp

Model-assisted clustering for automated operational modal analysis of partially continuous multi-span bridges

Elisa Tomassini [a], Enrique García-Macías [b,*], Edwin Reynders [c], Filippo Ubertini [a]

[a] Department of Civil and Environmental Engineering, University of Perugia, Via G. Duranti, 93 06125 Perugia, Italy
[b] Department of Structural Mechanics and Hydraulic Engineering, University of Granada, Campus de Fuentenueva s/n, 18071 Granada, Spain
[c] Department of Civil Engineering, University of Leuven (KU Leuven), Kasteelpark Arenberg 40, B-3001 Leuven, Belgium

ARTICLE INFO

Communicated by S. Laflamme

Keywords:
Analytical solution
Damage identification
Hierarchical clustering
Multi-span bridges
Operational Modal Analysis
Periodic structures
Structural Health Monitoring

ABSTRACT

Long multi-span bridges represent a broad section of the civil roadway infrastructure. Despite being so common, their condition-based maintenance through vibration-based Structural Health Monitoring (SHM) has been scarcely investigated in the literature. The dynamic identification of such structures through Operational Modal Analysis (OMA) is especially challenging due to of their quasi-periodic nature and the common existence of weak inter-span coupling. Even when designed following an isostatic scheme, there always exists a certain degree of coupling between spans due to the continuity of the deck, the pavement and imperfect expansion joints. Hence, the modal poles of the spans typically appear as dense clusters with closely spaced frequencies and mode shapes with similar wavelengths, which significantly hinders the identification of physical poles through stabilization diagrams. In this light, this paper proposes a model-based machine learning approach to conduct and interpret the OMA results of partially continuous multi-span bridges. The proposed method is a hierarchical clustering approach that leverages on the analytical solution of the vertical free vibration response of multi-span girders with weak inter-span rotational coupling, allowing the estimation of the modal features of any bridge configuration ranging from simply supported to perfectly continuous conditions. Detailed parametric analyses and discussions are presented to appraise the correlation between the inter-span rotational coupling and the clustering of the modal poles of multi-span bridges, as well as the influence of damage conditions of varying severity and extension. On this basis, a model-based cut-off distance threshold for hierarchical clustering of stable poles is proposed to assist the automation of the global OMA of multi-span bridges. The developed formulation is tested in a real-world in-operation seven-spans reinforced concrete girder bridge, the Trigno V Bridge in Italy.

1. Introduction

Over the past decade, increasing efforts have been made worldwide to find efficient ways to reduce the number of structurally deficient bridges and improve their safety. These efforts are motivated by the serious economic and life losses resulting from the failure of these critical elements of the transportation network. A prominent example is the collapse of the Tuojiang Bridge (Hunan, China) in 2007 during its construction, which caused 66 fatalities and 23 injured [1]. Another recent case is the tragic collapse of the Morandi Bridge (Genoa, Italy) in 2018 [2], which caused 43 casualties, the evacuation of 600 people, and estimated costs in

* Corresponding author.
E-mail addresses: elisa.tomassini1@studenti.unipg.it (E. Tomassini), enriquegm@ugr.es (E. García-Macías), edwin.reynders@kuleuven.be (E. Reynders), filippo.ubertini@unipg.it (F. Ubertini).

https://doi.org/10.1016/j.ymssp.2023.110587
Received 2 March 2023; Received in revised form 22 May 2023; Accepted 3 July 2023
Available online 19 July 2023

damages around €400–600 million [3]. In the U.S., the American Society of Civil Engineers (ASCE) points out that 42% of the 617 thousands American road bridges are at least 50 years old and 7.5% of them present structural deficiencies [4]. This is consistent with other recent statistics reporting a total of 1062 bridge failures in the US between 1980 and 2012 [5]. In China, recent studies point out that 69.6% of the bridge failures are due to anthropic factors, inadequate maintenance and supervision representing primary causes [6]. The response by governments to such a pressing challenge is being reflected in increasing investments in infrastructure resilience and the enactment of advanced SHM regulations in recent years. In China, the Ministry of Transportation issued in 2014 the Technical Code for SHM of buildings and bridges (GB50982) and in 2016 the design code for SHM systems for large highway bridges (JT/T1037) [7]. In May 5th 2022, the Federal Highway Administration (FHWA) of U.S. Department of Transportation announced an additional $1.14 billion in funding for bridge rehabilitation and replacement as well as in updating the National Bridge Inspection Standards (NBIS) [8]. In the European context, despite the absence of a pertinent legislation beyond recommendations, the European Commission has invested considerable R&D efforts into the field of SHM [9]. Among the EU countries, the guidelines for Risk Classification and Management of Bridges issued by the Italian Ministry of Infrastructure and Transport in 2020 and then updated on July 1st 2022 [10] represent the most recent technical code highlighting the pivotal role of SHM for the management of ageing infrastructure.

Legislation on bridge inspection and maintenance has been driven by a considerable volume of research in the last decades on the development of algorithms and solutions to monitor and control the integrity of civil engineering structures. Such developments fall within the framework of SHM which, in opposition to traditional periodically scheduled maintenance models, advocates the implementation of non-destructive continuous monitoring solutions to enable preventive maintenance [11]. Among the wide variety of existing monitoring technologies, vibration-based SHM based on OMA has become particularly popular owing to its global assessment capabilities, minimum intrusiveness, and relatively easy automation [12,13]. These techniques allow extracting the modal features of a structural system (i.e. resonant frequencies, damping ratios and mode shapes) by exploiting acceleration response time series under normal operating conditions [14]. Given their dependency upon the stiffness and the energy dissipation mechanisms of structures, modal features can be used to identify the appearance of damage [15,16]. Since OMA techniques do not require to interrupt the traffic flow and sensors can be typically secured in areas of the structure non-accessible by users, a considerable number of successful applications to both railway [17,18] and highway [19,20] bridges have been reported in the literature. Considerable efforts have been also devoted to the development of efficient techniques capable of achieving high damage classification levels (detection, localization and quantification) through continuous vibration-based SHM. The most recent advances include, among others, continuous supervised damage identification through surrogate modelling [21] and Artificial Intelligence (AI) [22], AI-based OMA techniques [23], transfer learning and population-based SHM [24].

As a cornerstone to enable the implementation of OMA into continuous SHM schemes, considerable research efforts have been exerted in recent years to develop Automated OMA (AOMA) techniques. In particular, special attention has been devoted to the automation of time domain-based Stochastic Subspace Identification (SSI) methods [25,26]. These techniques typically address the automated interpretation of stabilization diagrams assessing the consistency of the identified poles of the system for increasing model orders [27]. Once clearly spurious/mathematical poles are removed according to hard (HC) and soft (SC) criteria, a certain clustering technique needs to be adopted to group the poles tagged as stable into subsets of similar modal features [28]. To this aim, a number of clustering approaches have been proposed in the literature, including hierarchical clustering [29], fuzzy clustering [30], Gaussian Mixture Models (GMM) [31], density-based clustering [30], and k-means [32]. Agglomerative (bottom up) hierarchical clustering techniques are widespread unsupervised machine learning algorithms given their insensitivity to initialization conditions, easy implementation, and simple interpretation of the hierarchical relation between clusters. The algorithm starts by considering all the poles form independent clusters. Afterwards, a hierarchical representation is created by sequentially merging pairs of clusters that are closest to each other until concentrating all the poles in one single cluster [33]. Linkages among poles are defined according to a certain distance metric accounting for their similarities in terms of resonant frequency and/or damping ratio as well as the orthogonality between their mode shape vectors. This process is finally represented in a dendogram rendering the tree-like structure of the hierarchical similarity among the poles of the system. On this basis, physical poles can be identified by those clusters compliant with a certain cut-off distance on the dendrogram, that is the limit linkage distance above which clusters will not be merged. Therefore, this user-defined distance threshold critically determines the quality of the outcome of the OMA. The problem of finding an optimal threshold to automate the clustering phase has been addressed by several authors in the literature. For instance, Reynders et al. [34] defined the optimal cut-off threshold through statistical moments extracted from an initial 2-means clustering step adopted to differentiate between possibly physical modes and certainly spurious modes. Similarly, Zini et al. [35] recently proposed the definition of the cut-off threshold as the 80th percentile of the minimum linkage distances determined over the sets of stable poles at every model order in the stabilization diagram.

In the context of OMA of bridge structures, long multi-span bridges represent particularly challenging systems. Such bridges, which constitute a sizeable portion of the bridge stock worldwide, typically present quasi-periodic configurations characterized by mechanical/geometrical repetitiveness and weak connections between consecutive spans. The prefix *quasi* is related to the frequent presence of slight differences between the connections and the properties of the spans. A certain degree of continuity is also common in the case of isostatic configurations as a result of weak deck/asphalt connections, imperfect expansion joints and/or stringers. In the field of railway bridges, the coupling may be due to the effect of rails and ballast continuity and considerable research has been reported on the analysis of weak coupling effects upon the dynamic response under moving loads (see e.g. [36,37]). Nonetheless, the number of works dealing with the OMA of multi-span bridges with weak coupling effects is considerably scarce. In this regard, the main difficulties stem from the fact that the modal properties of the spans typically appear as dense clusters of poles with closely spaced frequencies and mode shapes with similar wavelengths [38]. Only slight differences arise as a result of

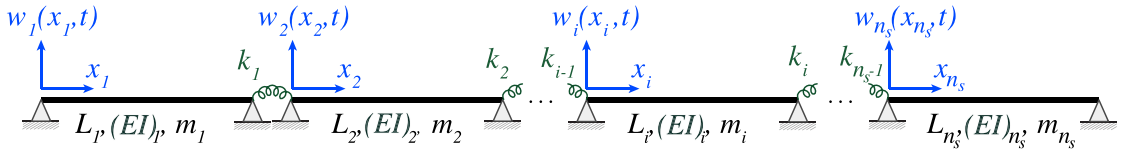

Fig. 1. Multi-span bridge divided into n_s simply supported spans with partial rotational coupling.

minor differences among spans and imperfect independence, which considerably hinders the identification of physical poles using standard stabilization diagrams. In this context, two different approaches are commonly adopted in practice: (i) to assume the spans are dynamically independent and conduct span-wise OMA (refer e.g. to [39]); (ii) to consider that there is a certain (unknown) degree of continuity and to perform a global identification (as e.g. [40]). Nonetheless, such approaches risk missing global vibration modes and confusing local and global modes, respectively. Among the few works in the literature coping with this issue, it is worth noting the contribution by Zhang et al. [41] who proposed an innovative approach based on a finite element model (FEM) updating approach exploiting free wave characteristics under forced excitation instead of modal signatures. While initially validated only in a simple lab structure, Zhang and co-authors [42] later verified the feasibility of free wave identification for the calibration of a FEM of the K032 viaduct (Bruges, Belgium) consisting of two 800 m long parallel curved bridges of 23 spans.

In light of the aforementioned gap in the literature, we propose in this paper a novel model-based clustering strategy for AOMA of multi-span bridges with weak inter-span rotational coupling. The proposed approach is based upon the closed-form solution of a multi-span Euler–Bernoulli beam model with rotational springs between adjacent spans. In this light, the optimal cut-off distance to be used for the hierarchical clustering of stable poles identified by OMA is set up according to frequency bands of the natural modes of vibration predicted by the developed theoretical model. Detailed parametric analyses are presented to evaluate the influence of the coupling degree between spans upon the clustering of poles in stabilization diagrams. Additionally, parametric analyses are also presented to investigate the influence of damage upon the modal features with respect to the reference (undamaged) condition in order to get some insights on which modes to track and inspect for damage detection purposes, considering the existence of as many closely spaced modes for each modal order as the number of spans. Finally, the effectiveness of the proposed approach is investigated in a real 7-span bridge, the Trigno V Bridge located in the region of Abruzos (Italy). The remainder of this paper is organized as follows. Section 2 presents the theoretical formulation of the developed multi-span Euler–Bernoulli beam model. Numerical results and discussion are presented in Section 3 and, finally, Section 4 ends the paper with some concluding remarks.

2. Theoretical framework: Multi-span Euler–Bernoulli beam model with rotational springs between adjacent spans

Let us assume a multi-span bridge as the composition of n_s Euler–Bernoulli simply supported beams of length L_i, $i = 1, \dots, n_s$, connected by linear rotational springs with stiffness constants k_j, $j = 1, \dots, n_s - 1$, governing the degree of rotational continuity between adjacent spans. The mass per unit length, m_i, and the flexural stiffness, $(EI)_i$, are assumed to be constant within every span. Finally, a local spatial coordinate x_i is defined along the ith beam element, i.e. $x_i \in [0, L_i]$ (see Fig. 1).

Under the hypothesis of undamped motion, the differential equation of vertical displacements $w_i(x_i,t)$ of the ith beam under free vibrations reads:

$$m_i \frac{\partial^2 w_i(x_i,t)}{\partial t^2} + \frac{\partial^2}{\partial x_i^2}\left[(EI)_i \frac{\partial^2 w_i(x_i,t)}{\partial x_i^2}\right] = 0. \tag{1}$$

Modal decomposition can be used to solve Eq. (1) by imposing $w_i(x_i,t) = \phi_i(x_i)q_i(t)$, with $\phi_i(x_i)$ and $q_i(t)$ denoting the mode shape and the corresponding generalized modal coordinate, respectively. Considering harmonic motions, the modal decomposition of Eq. (1) leads to the spatial differential equation:

$$\frac{\mathrm{d}^4\phi_i(x_i)}{\mathrm{d}x^4} - \alpha^4 \frac{m_i}{(EI)_i}\phi_i(x_i) = 0, \tag{2}$$

with

$$\alpha = \sqrt[4]{\omega^2 \frac{m_i}{(EI)_i}}. \tag{3}$$

The general solution of Eq. (2) reads [43]:

$$\phi_i(x_i) = C_i \cos(\alpha x_i) + D_i \sin(\alpha x_i) + E_i \cosh(\alpha x_i) + F_i \sinh(\alpha x_i). \tag{4}$$

The spanwise integration constants C_i, D_i, E_i, F_i in Eq. (4) are computed by imposing the boundary conditions reported in Table 1. These boundary conditions correspond to vanishing deflections at the supports, vanishing bending moments at the first and last supports, and continuity conditions of bending moments at each intermediate support. Note in Table 1 that the terms $\beta_i = \frac{k_i}{EI_i}$ quantify the rotational coupling between the spans. The derivation process is exposed in Appendix in which the boundary conditions

Table 1
Boundary conditions.

First support	Intermediate supports	Last support
$\phi_1(0) = \phi_1(L_1) = 0,$	$\phi_i(0) = \phi_i(L_i) = 0,$	$\phi_{n_s}(0) = \phi_{n_s}(L_{n_s}) = 0,$
$\phi_1''(0) = 0,$	$\phi_i''(L_i) = \phi_{i+1}''(0),$	$\phi_{n_s}''(L_{n_s}) = 0,$
$\phi_1''(L_1) = \phi_2''(0),$	$\phi_i''(L_i) = \beta_i(\phi_{i+1}'(0) - \phi_i'(L_i)),$	$\phi_{n_s}''(0) = \phi_{n_s-1}''\left(L_{n_s-1}\right),$

in Table 1 are imposed and the integration constants D_i, E_i and F_i are combined as a function of C_i. The modal coefficients C_i can be obtained by solving a system of $n_s - 1$ equations in the form:

$$\begin{bmatrix} \varphi_1 + \varphi_2 + 2\frac{\alpha}{\beta_1} & -\psi_2 & 0 & \cdots & 0 \\ -\psi_2 & \varphi_2 + \varphi_3 + 2\frac{\alpha}{\beta_2} & -\psi_3 & \cdots & 0 \\ 0 & -\psi_3 & \varphi_3 + \varphi_4 + 2\frac{\alpha}{\beta_3} & \cdots & 0 \\ \vdots & \vdots & \vdots & \ddots & \vdots \\ 0 & 0 & 0 & \cdots & \varphi_{n_s-1} + \varphi_{n_s} + 2\frac{\alpha}{\beta_{n_s-1}} \end{bmatrix} \begin{bmatrix} C_2 \\ C_3 \\ C_4 \\ \vdots \\ C_{n_s} \end{bmatrix} = \boldsymbol{\Gamma}_{n_s-1}\,\mathbf{C} = \mathbf{0}, \tag{5}$$

The term $\boldsymbol{\Gamma}_{n_s-1} \in \mathbb{R}^{(n_s-1)\times(n_s-1)}$ in Eq. (5) denotes the characteristic matrix and $\mathbf{C} \in \mathbb{R}^{n_s-1}$ is a vector containing the coefficients C_i. Imposing for the sake of simplicity, that all the spans have the same mechanical properties, mass properties and equal length, the i sub-index can be dropped from the characteristic matrix as:

$$\boldsymbol{\Gamma}_{n_s-1} = \begin{bmatrix} 2\left(\varphi + \frac{\Lambda}{\beta L}\right) & -\psi & 0 & \cdots & 0 \\ -\psi & 2\left(\varphi + \frac{\Lambda}{\beta L}\right) & -\psi & \cdots & 0 \\ 0 & -\psi & 2\left(\varphi + \frac{\Lambda}{\beta L}\right) & \cdots & 0 \\ \vdots & \vdots & \vdots & \ddots & \vdots \\ 0 & 0 & 0 & \cdots & 2\left(\varphi + \frac{\Lambda}{\beta L}\right) \end{bmatrix}, \tag{6}$$

where a non-dimensional coefficient $\Lambda = \alpha L$ has been introduced. The existence of non-trivial solutions requires:

$$\det\left(\boldsymbol{\Gamma}_{n_s-1}\right) = 0, \tag{7}$$

which represents the characteristic equation for the solution of the eigenvalues Λ. Considering the tridiagonal structure of $\boldsymbol{\Gamma}_{n_s-1}$ in Eq. (6), it is possible to find a closed-form expression for its determinant through the recurrence relation given by the Laplace expansion as [44]:

$$\det\left(\boldsymbol{\Gamma}_{n_s-1}\right) = 2\left(\varphi + \frac{\Lambda}{\beta L}\right)\boldsymbol{\Gamma}_{n_s-2} - \psi^2 \det(\boldsymbol{\Gamma}_{n_s-3}), \tag{8}$$

where $\boldsymbol{\Gamma}_{n_s-2}$ and $\boldsymbol{\Gamma}_{n_s-3}$ are the minors of $\boldsymbol{\Gamma}$ of order $n_s - 2$ and $n_s - 3$. From the recursive expression in Eq. (8), it can be extracted:

$$\det\left(\boldsymbol{\Gamma}_{n_s-1}\right) = \frac{a_1^{n_s} - a_2^{n_s}}{a_1 - a_2}, \tag{9}$$

where:

$$\begin{aligned} a_1 &= \varphi + \beta^{-1}\left[\frac{\Lambda}{L} + \sqrt{\left(\frac{\Lambda}{L}\right)^2 + \beta^2\left(\varphi^2 - \psi^2\right) + \frac{2\Lambda\beta\varphi}{L}}\right], \\ a_2 &= \varphi + \beta^{-1}\left[\frac{\Lambda}{L} - \sqrt{\left(\frac{\Lambda}{L}\right)^2 + \beta^2\left(\varphi^2 - \psi^2\right) + \frac{2\Lambda\beta\varphi}{L}}\right]. \end{aligned} \tag{10}$$

Note that Eq. (7) constitutes a transcendental equation and, therefore, it has to be solved numerically. Once solved, vector $\mathbf{C}$ for the n-th mode can be obtained by solving the linear system of equations for the corresponding Λ_n solution. The n-th natural frequency, f_n, can be evaluated by back substitution into Eq. (3):

$$f_n = \frac{\Lambda_n^2}{2\pi L^2}\sqrt{\frac{EI}{m}}. \tag{11}$$

To complete the definition of the mode shapes, the remaining coefficients E_i, D_i, and F_i can be computed from Eqs. ((A.1),(A.7)) in Appendix. For the first span, the boundary conditions in Table 1 lead to $C_1 = E_1 = 0$, while D_1 and F_1 can be easily extracted by imposing $\phi_1''(L_1) = \phi_2''(0)$. Similarly, the coefficients for the last span can be extracted by imposing the boundary conditions in Table 1. Then, the nth mode shape along an arbitrary ith span reads:

$$\phi_{n,i}(x_i) = \frac{C_{n,i}}{X_n}\left(\cos\left(\alpha_n x_i\right) - \cosh\left(\alpha_n x_i\right)\right) + \frac{D_{n,i}}{X_n}\sin\left(\alpha_n x_i\right) + \frac{F_{n,i}}{X_n}\sinh\left(\alpha_n x_i\right), \tag{12}$$

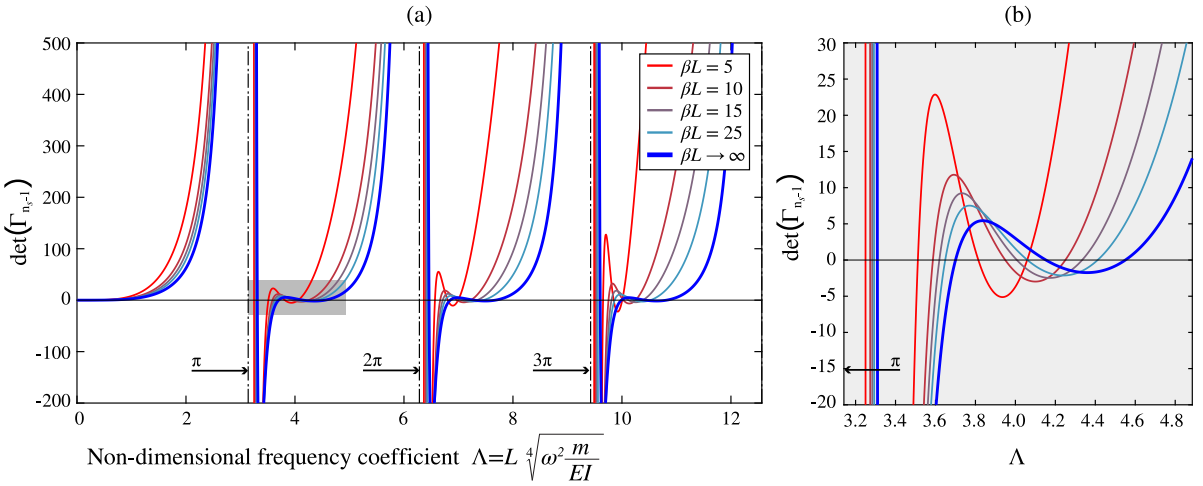

Fig. 2. Determinant of the characteristic matrix $\boldsymbol{\Gamma}_{n_s-1}$ for a bridge with $n_s = 5$ spans versus the non-dimensional frequency parameter Λ (a), and detailed view of the first block of solutions corresponding to the first order bending modes (b).

with X_n being a scale factor that can be obtained by imposing mass-normalization of the global mode shape as:

$$\sum_{i=1}^{n_s}\int_0^{L_i} m\phi_i(x_i)^2 \mathrm{d}x_i = \frac{m}{X_n^2}\sum_{i=1}^{n_s}\int_0^{L_i}\left[C_{n,i}\left(\cos\left(\alpha_n x_i\right)-\cosh\left(\alpha_n x_i\right)\right)+D_{n,i}\sin\left(\alpha_n x_i\right)+F_{n,i}\sinh\left(\alpha_n x_i\right)\right]^2 \mathrm{d}x_i = 1. \tag{13}$$

The solution of X_n can be extracted from Eq. (13) as:

$$X_n = \sqrt{\sum_{i=1}^{j} m\left(Y_1^n + Y_2^n + Y_3^n + Y_4^n\right)}, \tag{14}$$

where the expressions for coefficients Y_i^n read:

$$Y_1^{n,i} = 2\left[-C_i\left(D_i+F_i\right)+l_i\alpha_n\left(2C_i^2+D_i^2-F_i^2\right)\right], \tag{15a}$$

$$Y_2^{n,i} = -2C_iD_i\cos\left(2l_i\alpha\right)+\left(C_i^2-D_i^2\right)\sin\left(2l_i\alpha\right), \tag{15b}$$

$$Y_3^{n,i} = -2C_iF_i\cosh\left(2l_i\alpha\right)+\left(C_i^2+F_i^2\right)\sinh\left(2l_i\alpha\right), \tag{15c}$$

$$Y_4^{n,i} = 4\cosh\left(l_i\alpha\right)\left[C_i\left(D_i+F_i\right)\cos\left(l_i\alpha\right)+\left(D_iF_i-C_i^2\right)\sin\left(l_i\alpha\right)\right], \tag{15d}$$

$$Y_5^{n,i} = 4\sinh\left(l_i\alpha\right)\left[-\left(C_i^2+D_iF_i\right)\cos\left(l_i\alpha\right)+C_i\left(F_i-D_i\right)\sin\left(l_i\alpha\right)\right]. \tag{15e}$$

3. Validation studies and discussion

This section presents a detailed study of the structure and potential of the analytical solution presented above to conduct AOMA of multi-span bridges with weak rotational coupling conditions. Specifically, Section 3.1 analyzes the structure of the characteristic equation in Eq. (7), as well as the dependency of the modal properties with the number of spans n_s and the rotational coupling factor β. Afterwards, Section 3.2 investigates the effects of damage with varying severity and extension upon the modal properties. Finally, Section 3.3 illustrates the usefulness of the developed analytical solution to assist the AOMA of a real in-operation multi-span bridge.

3.1. Parametric analysis of the analytical model

Let us first inspect the relationship between the parameter βL, henceforth referred to as the *connection degree*, and the characteristic equation in (7). The connection degree βL is a non-dimensional factor representing the ratio between the stiffness of the rotational springs k and the flexural stiffness of the beams EI/L. In this light, Fig. 2(a) depicts the determinant of the characteristic matrix $\boldsymbol{\Gamma}_{n_s-1}$ for a 5-span bridge ($n_s = 5$) with increasing continuity degrees, spanning from $\beta L = 5$ until $\beta L \to \infty$ (perfect rotational continuity). It is first noted in Fig. 2(a) that the determinant of the characteristic matrix presents equally spaced vertical asymptotes at $\Lambda = n\pi$, $n \in \mathbb{N}$. These asymptotes correspond to the limit $\beta L \to 0$, for which Eq. (7) becomes indeterminate. This limit case corresponds to the pure isostatic configuration without any rotational coupling between spans, whose solutions turn into $\omega_n = n^2\pi^2\sqrt{EI/mL^4}$ [45], i.e. $\Lambda = n\pi$. Considering the asymptotes, the characteristic equation (7) presents blocks of $n_s = 5$ roots. It can be seen in the detailed view of the first block in Fig. 2(b) that the roots increase with increasing connection degree βL.

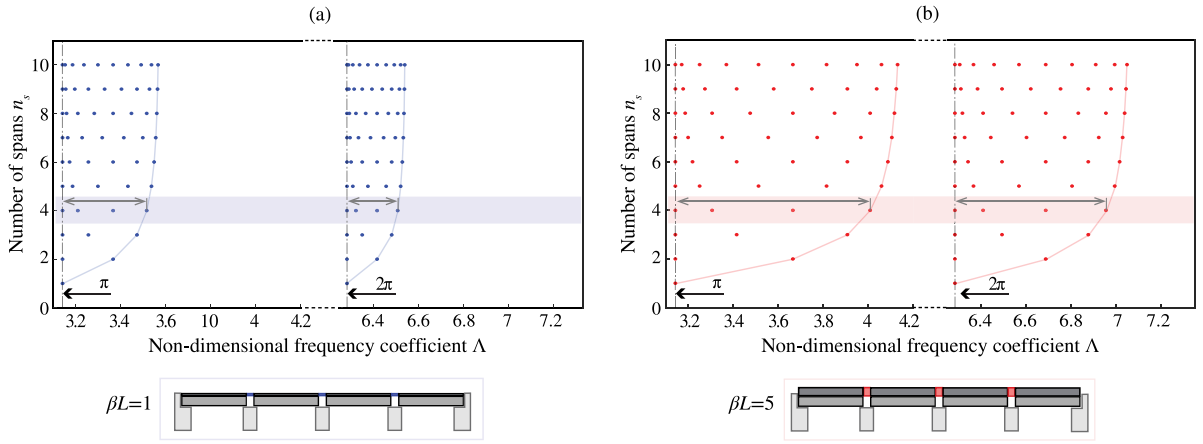

Fig. 3. First two blocks of roots of the characteristic matrix of multi-span beams with an increasing number of spans n_s considering two different rotational coupling degrees, namely $\beta L = 1$ (a) and $\beta L = 5$ (b).

The blocks of solutions corresponding to the 1st and 2nd order bending modes versus the non-dimensional frequency parameters Λ are further investigated in Fig. 3 for an increasing number of spans n_s. In order to appraise the effect of the inter-span rotational coupling, two different βL values of 1 and 5 are considered in Fig. 3(a) and (b), respectively. It is clear in these figures that the roots fall between the vertical lines at π and 2π and exponential-like envelopes. The vertical lines at integer multiples of π represent the isostatic solutions which always exist also in partially-continuous or continuous configurations, being therefore invariant with respect to βL. The envelopes, instead, depend upon βL. As the number of spans increases, the rate of increase of the envelopes tends to stabilize leading to a denser clustering of the solutions. Furthermore, note that the gap between the solutions expands as the rotational coupling increases. Therefore, the separation between the resonant frequencies of the modes of a multi-span bridge belonging to a certain bending mode order ranges between the limit configurations of $\beta L \to 0$ (purely isostatic with no rotational coupling between the spans leading to n_s spanwise modes with the same natural frequency $\Lambda = n\pi$) and $\beta L \to \infty$ (perfectly continuous configuration). A conclusion of practical interest from this analysis regards the dependency between the frequency range covered by the solutions belonging to a certain model order (or alternatively, the envelope curve) and the degree of inter-span rotational coupling. In this light, it may be possible to collect abacuses of envelope curves to infer the rotational coupling degree from experimentally determined modal poles.

The envelope curves for the first bending modal order considering different coupling degrees βL and number of spans n_s are presented in Fig. 4(a) and (b), respectively. Note in Fig. 4(a) that all the envelopes start at the solution for the isostatic configuration ($\Lambda = \pi$) and exhibit increasing growth rates as the rotational coupling increases. Specifically, the largest growth rates are observed for coupling factors above $\beta L = 1$ until achieving convergence to the solution of the continuous multi-span model, not finding significant growths for coupling degrees above $\beta L = 100$. On the other hand, when keeping constant the number of spans n_s and varying the coupling degree βL, Fig. 4(b) highlights that the variation of the width of the envelope curves sensibly depends on the number of spans n_s. It is also noticeable in this figure that the rotational coupling βL required to achieve convergence to the continuous multi-span framework depends upon the number of spans n_s. For instance, convergence for curves corresponding to the cases of 2 and 3 spans is approximately achieved for βL coefficients larger than 60 and 100, respectively. This behaviour is explained by the fact that, as the number of spans n_s increases, the coupling stiffness required to guarantee the rigid rotation of the section over the supports must be larger.

The mode shapes (normalized to a unit maximum amplitude) obtained for 4-span beams with rotational coupling degrees of $\beta L = 0$ (a), $\beta L = 5$ (b) and $\beta L \to \infty$ (c) are shown in Fig. 5. In the case of isostatic configuration ($\beta L = 0$) in Fig. 5(a), each span is independent and two sets of four repeated eigenvalues are found. In addition, the local eigenfunctions evaluated at each span present identical wavelengths. As the rotational coupling differs from zero, the eigenfunctions tend to converge to the continuous configuration ($\beta L \to \infty$) in Fig. 5 (c). Indeed, the eigenfunctions identified for the case of intermediate coupling ($\beta L = 5$) are indistinguishable from those of the continuous configuration as evidenced by the modal assurance criterion (MAC) matrix furnished in Fig. 6(a). In this figure, the modal displacements are evaluated at $L/4$, $L/2$ and $3L/4$, as commonly adopted in practice. The MAC is a metric assessing the orthogonality between two eigenvectors [46], with values of 0 and 1 indicating perfect independence (orthogonal) and perfect correlation (linearly dependent), respectively. The quasi-diagonal structure of the MAC matrix in Fig. 6(a) confirms that the eigenvectors for $\beta L = 5$ and $\beta L \to \infty$ are almost identical. The small residuals in the off-diagonal terms are due to slight discrepancies that appear in the areas adjacent to the supports and limitations in the sampling of the eigenvectors. Also in cases where βL is less than 1, the modes still tend to be very similar to those of the continuous case, and the slightest differences are localized areas nearby the supports. Note in Fig. 5(b) and (c) that modes 1–4 and 5–8 respectively exhibit identical wavelengths, differing only in terms of relative maximum amplitude among the spans. Along with the circumstance that mode shapes are only evaluated at a limited number of locations in practice, with the subsequent lower accuracy compared

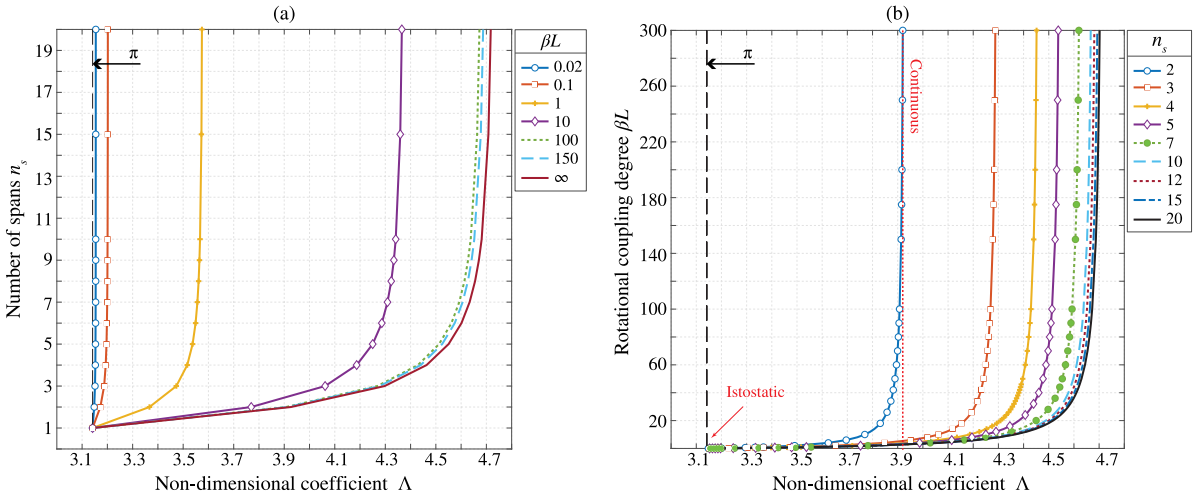

Fig. 4. Abacuses of the envelopes of the first order bending mode solutions: (a) Λ versus n_s, (b) Λ versus βL.

to resonant frequencies [47], small inaccuracies in the identification of the mode shapes (e.g. imperfect sensor synchronization or alignment) may lead to erroneous modal classifications when using the MAC metric. In the cases of partially continuous and continuous configurations, it is worth stressing the fact that the first eigenvalues are very close (the first one is nearly identical) to those of the perfectly isostatic scheme ($\Lambda = n\pi$). Furthermore, it is important to remark that the local eigenfunctions observed in the isostatic configuration exhibit identical wavelengths to those found for the partially coupled and continuous configurations. This analysis is deepened in Fig. 6(b), which reports the MAC values between the local modes 1 and 2 extracted for the fourth and the third spans of the beam with isostatic configuration with the corresponding local modes extracted from the $\beta L = 5$ and $\beta L \to \infty$ configurations. It is noted in this figure that the first local mode from the isostatic case is locally almost parallel and perpendicular to modes 1–4 and 5–8 of the partially coupled and continuous configurations, respectively, and vice versa for the second mode (small inaccuracies in MAC calculations are due to spatial sampling of the eigenfunctions to get the eigenvectors). These results are of high practical interest since they highlight the risk of confusing local and global modes when performing span-wise OMA of multi-span bridges.

3.1.1. *Discussion and development of model-assisted distance metric for AOMA*

Consequences of the previous parametric analyses from a OMA perspective can be listed as follows:

- The resonant frequencies of n_s-span bridges with weak inter-span rotational coupling appear in blocks of n_s poles bounded between the natural frequencies of the isostatic configuration ($\Lambda = n\pi$, $n \in \mathbb{N}$), which always exist, and envelope curves depending upon βL.
- The spacing in frequency among the n_s poles is a function of the inter-span rotational coupling degree βL. In general, the spacing between the solutions decreases as the number of spans n_s increases and the coupling degree βL diminishes.
- The frequency bandwidth of the clusters of poles belonging to a certain bending mode order in a stabilization diagram can be used to infer the inter-span rotational coupling βL of multi-span bridges.

In the context of OMA, the physical meaningfulness of identified poles of the system is typically assessed through a stabilization diagram. Stabilization diagrams depict the identified poles (typically in terms of frequency) for all the considered model orders. On this basis, the physical (true) poles of the monitored structure are found as alignments of poles consistently identified throughout the considered range of model orders. The dissimilarity between the poles is commonly assessed through a certain distance metric formulated in terms of resonant frequencies and mode shapes such as [48]:

$$d_{ij}^{m} = \eta_1 \frac{|f_i^m - f_j^{m-1}|}{\max(f_i^m, f_j^{m-1})} + \eta_2 \left[1 - MAC\left(\boldsymbol{\phi}_i^{m-1}, \boldsymbol{\phi}_j^{m}\right)\right], \tag{16}$$

where f_j^{m-1} and f_i^m stand for the i-th and the j-th resonant frequencies of two poles identified at two adjacent model orders $m-1$ and m, respectively, $\boldsymbol{\phi}_j^{m-1}$ and $\boldsymbol{\phi}_i^m$ are the corresponding eigenvectors, and η_1 and η_2 denote weighing factors. The clustering algorithm starts by considering all the stable poles from the stabilization diagram as single clusters. Then, the algorithm computes the distance between all the stable poles according to Eq. (16), and groups the two closest clusters into a single cluster. The algorithm proceeds iteratively until all the poles are grouped into one single cluster. Finally, the dendogram summarizing the tree-like hierarchical structure of the clusters is cut at a certain cut-off distance threshold $\overline{d}$, so enabling the automation of the interpretation of the stabilization diagram for AOMA.

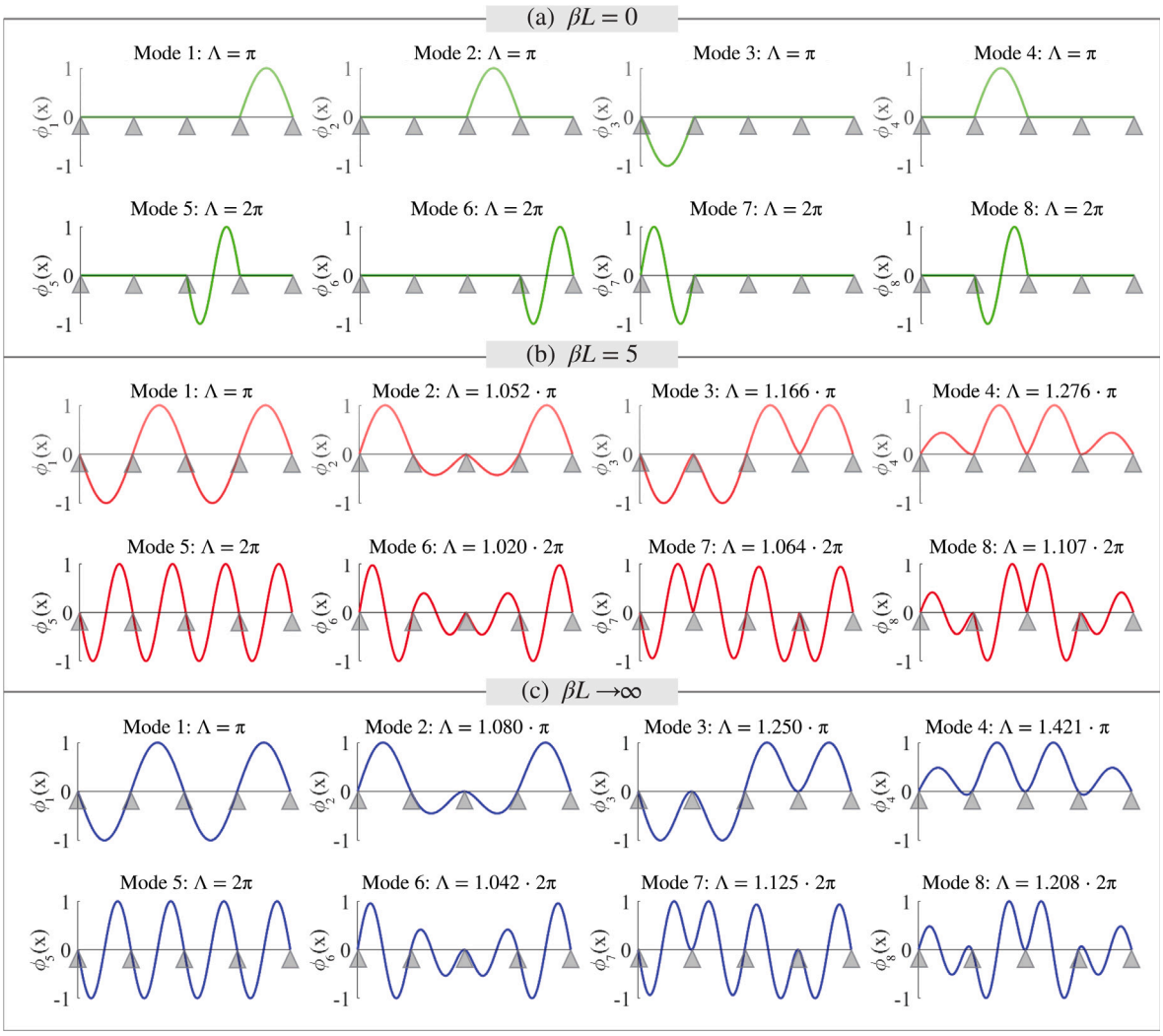

Fig. 5. First eight bending modes of 4-spans bridge with inter-span rotation coupling coefficients of $\beta L = 0$ (a), $\beta L = 5$ (b), and $\beta L \to \infty$ (c).

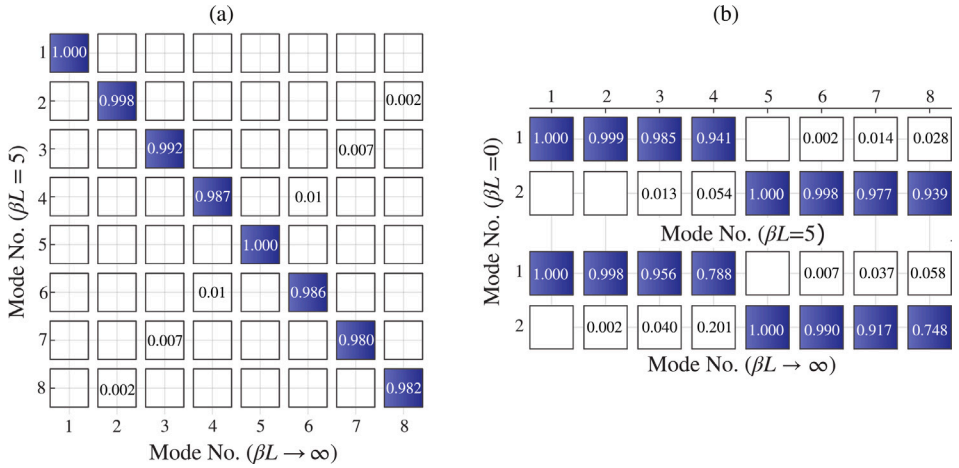

Fig. 6. (a) MAC matrix between the first eight eigenvectors determined for the 4-spans partially continuous ($\beta L = 5$) and continuous configurations ($\beta L = \infty$). (b) MAC matrix between the first two local modes determined for the isostatic configuration and the (locally evaluated) first eight modes determined for $\beta L = 5$ and $\beta L = \infty$. The eigenvectors are sampled at three points per span, namely $L/4$, $L/2$ and $3L/4$.

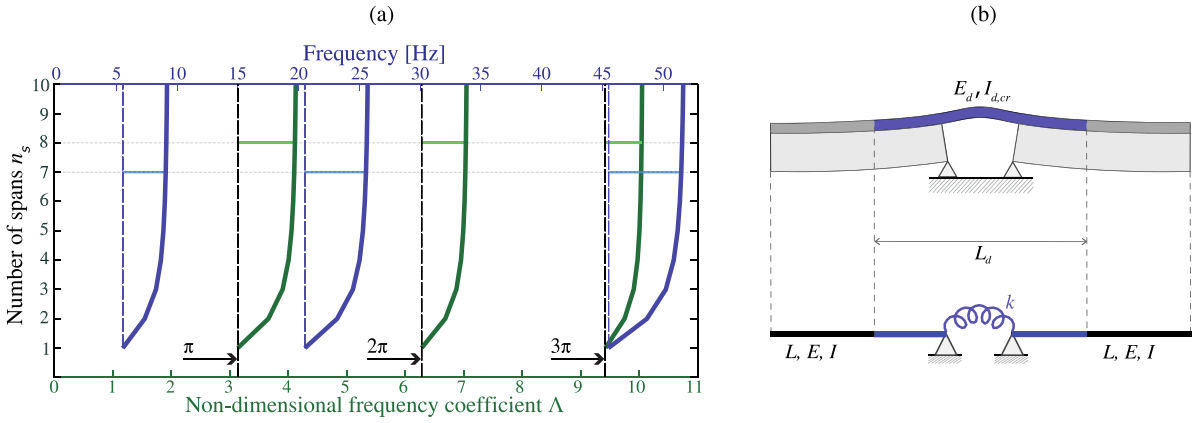

Fig. 7. Envelopes of the frequencies (blue) and of the non-dimensional coefficients Λ for the case of $\beta L = 5$ (a) and link deck schematization (b). (For interpretation of the references to colour in this figure legend, the reader is referred to the web version of this article.)

When conducting AOMA of multi-span bridges, it is possible to exploit the previously introduced analytical model to tune the cut-off distance $\overline{d}$ to be used in a hierarchical clustering algorithm. From the previous analyses, and with the purpose of avoiding potential misclassifications due to imperfect identification of mode shapes, the cut-off distance is formulated solely in terms of resonant frequencies ($\eta_1 = 1$, $\eta_2 = 0$). Specifically, to prevent the possibility of clustering two different closely-spaced modes belonging to the same model order and even the possibility of a mode being split into several neighbouring clusters, the cut-off distance threshold is set to the average frequency gap among the roots of the characteristic matrix from Eq. (3) belonging to the narrowest envelope. It is important to remark that the width of the envelopes increases as the order of the bending modes increases, thereby the clustering of poles intensifies as one aims to identify low order vibration modes as illustrated in Fig. 7(a). Note that this is not in contrast with the behaviour previously reported in Fig. 3, as that figure was referring to the non-dimensional frequency parameter Λ. Resonant frequencies ω are proportional to the square of Λ and, therefore, the width of the frequency envelopes is proportional to the difference of the squares of the maximum and minimum Λ solutions of the same modal order. Therefore, since the narrowest envelopes are those corresponding to the roots belonging to first order bending modes, the cut-off distance $\overline{d}$ can be defined as a function of the theoretical frequencies extracted from Eq. (7) as:

$$\overline{d} = \frac{1}{n_s - 1} \sum_{i=1}^{n_s - 1} \frac{f^t_{1,i+1} - f^t_{1,i}}{f^t_{1,i+1}}, \tag{17}$$

where $f^t_{1,i}$ and $f^t_{1,i+1}$ are the i-th and the $(i+1)$-th adjacent theoretical frequencies estimated for the block of solutions corresponding to the first order bending modes. Note that, while the mechanical and geometrical properties of multi-span bridges can in practice be estimated relatively well from the available information, the inter-span rotational coupling k will be commonly unknown. Let us assume the common configuration of multi-span bridges consisting of simply supported girders connected by a continuous deck as sketched in Fig. 7(b). In this case, to accurately describe the rotational stiffness of the link deck, it is important to consider two main phenomena [49]: (i) continuous decks typically debond from the main girders to accommodate the rotations at the supports; (ii) the cross-section of the deck in the areas close to the joints are typically cracked. Hence, the link deck can be conceived as a beam with length corresponding to the total debonded length L_d, and Young's modulus and cracked inertia with respect to the centre of gravity of the cross-section of the bridge given by E_d and $I_{d,cr}$, respectively. Based on experiments, Au et al. [49] found that the total debonded length L_d can be evaluated as the 5% of the sum of the lengths of the adjoining girders. Therefore, L_d is equal to $0.1L$ in the case in which all the spans have the same length. Additional considerations made in the validation of L_d were that the link deck introduced a negligible continuity to the structure because of its relatively low stiffness and tensile cracks were observed at the top of the link slab induced by negative bending moments. Therefore, these considerations support the case of a weak connection performed by the springs of the theoretical model and the employment of the cracked cross-section characteristics of the deck. On this basis, as a first approximation for girder multi-span roadway bridges with continuous decks, the rotational coupling can be estimated as:

$$k = \frac{2E_d I_{d,cr}}{L_d}, \tag{18}$$

and the inter-span rotational coupling degree βL can be defined as:

$$\beta L = 2\frac{(E_d I_{d,cr})/(EI)}{L_d/L}. \tag{19}$$

One last quality check related to the outcome of the hierarchical clustering phase regards the minimum number of poles forming a cluster to be considered as a physical mode. Ideally, for every model order, it is desirable to choose the n_s most populated (highest

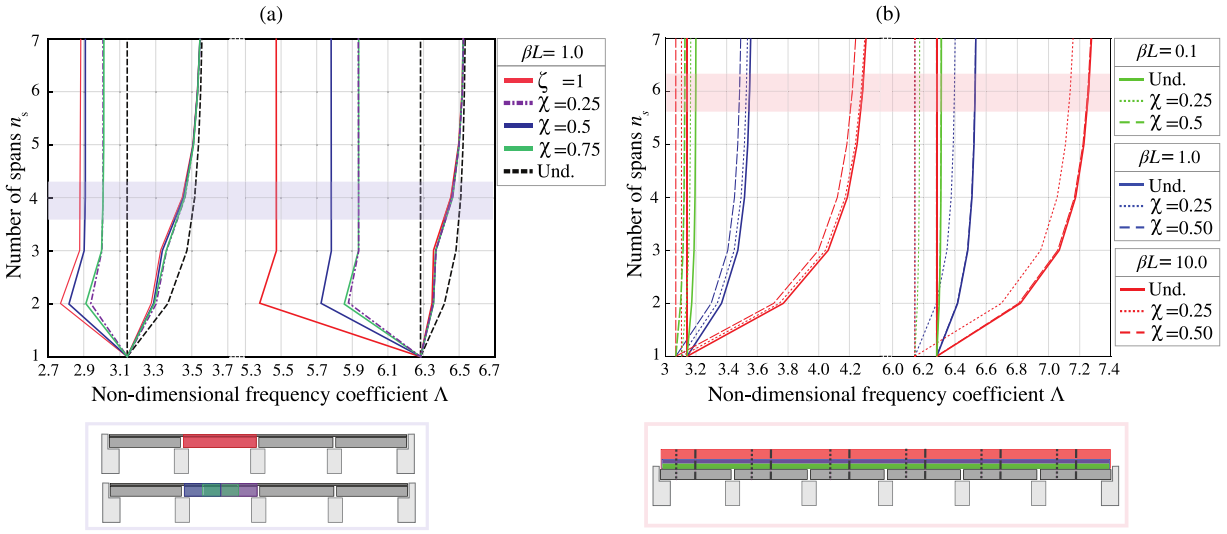

Fig. 8. Parametric analysis of the envelopes of the first and second order roots of multi-spans beams for damage conditions affecting large sections of the spans. (a) Damage of extension $\zeta = 0.5$ and intensity $\eta = 0.5$ affecting the second span $S = [2]$ at different positions χ (the case of degradation of the whole span $\zeta = 1$ is also included for comparison purposes). (b) Damage affecting all the spans $S = [1, \dots, n_s]$ at positions $\chi = \{L/4, L/2\}$ with extension $\zeta = 0.05$ and intensity $\eta = 0.5$ for different coupling degrees $\beta L = \{0.1, 1, 10\}$. (For interpretation of the references to colour in this figure legend, the reader is referred to the web version of this article.)

cluster sizes) clusters. The cluster size of the modes may depend on how the bridge is stressed by the traffic during the acquisitions and the participating mass in each mode, then clusters belonging to different modal order may present different sizes. Therefore, a reasonable way to choose the n_s modes belonging to the same modal order may be to select those presenting similar cluster sizes.

3.2. Parametric study on damage assessment: location and severity

The relatively large number of closely spaced modes per modal order hinders the damage identification of both localized and extensive defects, as well as the tracking of the most damage-sensitive modes. In fact, the possibility of characterizing damage increases if one is able to determine which of the n_s modes of each modal order is the most damage sensitive, so as to focus on it and narrow the field of analysis.

In this light, this section presents thorough parametric analyses to analyse the effects of damage conditions with varying severity and extension on the modal properties of multi-span bridges. To do so, the previous analytical model is formulated in a FEM using 2-nodes, 2 degrees of freedom (DOFs) per node, linear Euler–Bernoulli elements connected by rotational springs linking the rotational DOFs of nodes converging into the internal supports. For the purpose of achieving maximum accuracy, each span is discretized into 100 elements. Based upon the discretized model, damage is defined by affecting the flexural stiffness of certain elements. Specifically, damage is characterized by four different parameters:

- *Intensity*: $\eta = EI^d/EI \in [0, 1]$ with EI^d standing for the flexural stiffness of the damaged area.
- *Extension*: $\zeta = \Delta L/L \in [0, 1]$ where ΔL denotes the length of the damaged section.
- *Position*: $\chi = x/L \in \left[\frac{\zeta}{2}, 1 - \frac{\zeta}{2}\right]$, x being the central abscissa in which the damage is located with respect to the initial section of the span.
- *Damage location*: Vector $S = \left[s^{(1)}, \dots, s^{(n)}\right]$ with $1 \leq s^{(i)} \leq n_s \in \mathbb{N}$ determining the ith damaged span.

In the following analyses, the effects of damage are characterized in terms of how the envelopes of the roots of the characteristic equation diverge from the reference undamaged condition (labelled henceforth with "Und".). The attention focuses on two damage identification levels with practical interest in SHM of bridges: the ability to detect damage extended over large sections of the spans ($\zeta \geq 0.5$) and localized defects (e.g.$\zeta = 0.05$) in Figs. 8 and 9, respectively. The envelopes are evaluated for a maximum number of spans $n_s = 7$ for better visualization of the results.

Fig. 8 reports the results of the parametric analysis of damage affecting large sections of multi-span beams. On one hand, Fig. 8(a) investigates the effects of damage with an extension $\zeta = 0.5$ affecting the second span at different positions χ. The red solid envelopes denote the case in which the entire span is damaged ($\zeta = 1$). It is clear in this figure that damage induces a shifting of the divergence points between the branches of the envelopes towards lower values of frequency. Note the largest damage-induced effects are found when the damage is centred at the mid-span ($\chi = 0.5$), while very similar reductions are found for defects at positions $\chi = 0.25$ and $\chi = 0.75$. In these cases, only significant differences are observed for the 2-span cases, in which only the damage at $\chi = 0.25$ interferes with the rotational spring at the internal support. It is also interesting to remark that the damage-induced variations are

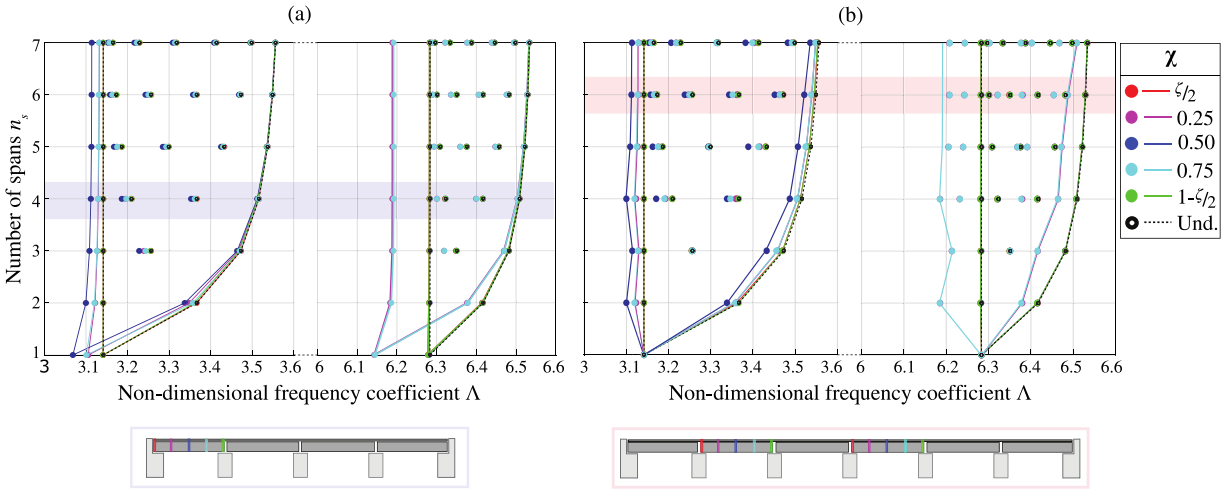

Fig. 9. Envelopes of the first and second order roots of multi-spans beams with rotational degree $\beta L = 1$ for two damage configurations considering different damage positions χ: (a) $\zeta = 0.05$, $\eta = 0.5$, $S = [1]$; (b) $\zeta = 0.05$, $\eta = 0.5$, $S = [2, 4]$. (For interpretation of the references to colour in this figure legend, the reader is referred to the web version of this article.)

more significant for the left branches of the envelopes. This is particularly evident for beams with a number of spans above 4, in which the right branches are almost coincident with the reference solution whilst the left branches experience an almost constant shift. In other words, this means that damage produces the largest effects on the mode whose natural frequency coincides with the isostatic simply supported case. When the damage is spread all throughout the beam in Fig. 8(b), a left translation of the envelopes takes place. The shift depends upon the position χ of the damage (independently of the coupling degree βL), achieving largest reductions in the first and second order bending modes when the defects are located at the mid-spans and at the quarter-spans, respectively. It is necessary to point out that since the variation is recursive in all the spans (the same decrease in stiffness is present in each span in the same position), that case can even be representative of the condition in which a recursive model deficiency occurs. In fact, if the model is not accurate and geometrical (periodical variation of the section) or physical (unmodelled masses, periodical variation of the stiffness) features are not well accounted for, the periodicity of the inaccuracies presented in all the spans can generate a translation of the left boundaries and a decrement of the right branches of the envelopes.

The second scenario investigating the effects of localized damage is reported in Fig. 9. In particular, Fig. 9(a) and (b) analyse the influence of damage when only located in the first span ($S = [1]$) and in the second and fourth spans $S = [2, 4]$, respectively. In these cases, the rotational coupling degree is set to $\beta L = 1$, and the intensity and extension of the defects is fixed to $\eta = 0.5$ and $\zeta = 0.05$. Lines and scatter points of different colours represent the roots obtained considering defects at different positions χ, while the black dashed lines and scatter points refer to the reference solution ("Und".). In these cases, note that the presence of damage mostly affects the left branches. Indeed, as the number of spans increases, the right branches quickly converge to that of the undamaged configuration. With regard to the location of damage, maximum damage-induced decreases in the left branches of the first and second order bending modes are found when the defects are located at the mid-span ($\chi = 0.5$) and at the quarter span ($\chi = \{0.25, 0.75\}$), respectively. When damage is located in one single span, as analysed in Fig. 9(a), it is observed that the induced shifts in the left branches of the envelopes decrease as the number of spans increases, achieving an almost constant value for beams with more than 4 spans. Contrarily, when spans 2 and 4 are affected by damage ($S = [2, 4]$), as reported in Fig. 9(b), the damage-induced shifts present a more irregular pattern, achieving maximum reductions in the left branches of the envelopes when the beams have two and four spans. It is necessary to point out that the simulations introduced in Figs. 8 and 9 are representative of high severity damages ($\eta = 0.5$). In fact, the purpose of the simulation was to highlight the effects of localized damages in frequencies. Obviously, in the case of a damage of lower severity, the frequencies will be less sensitive. In fact, frequencies tend to be more sensitive to extended damages rather than local defects, as also demonstrated in the recent work by Reynders et al. [50].

The previous analyses are complemented with the set of abacuses in Fig. 10 reporting the damage-induced frequency decays in the first and second order bending modes of a bridge composed by 4 spans with a connection degree $\beta L = 1$. The frequency decays in these figures are presented in non-dimensional form as Λ_i^d / Λ_i, $i = 1, \ldots, 8$, superscript "d" denoting the damage condition. Specifically, Fig. 10 furnishes the frequency decays induced by one single defect with extension $\zeta = 0.05$ in the first span $S = 1$ at positions $\chi = 0.5$ (Fig. 10(a)) and $\chi = 0.25$ (Fig. 10(b)) as the severity η varies. As it can be noted, the decay of the first frequency belonging to each modal order (Mode 1 and Mode 5 for the 1st and 2nd modal orders, respectively) is much greater than the others. It can also be seen that the span in which the damage is located presents larger modal displacements than the others, and the difference in amplitude increases with the extent ζ and intensity η of the damage. Therefore, it can be concluded that among the n_s modes of each modal order, the most sensitive to damage is the first one. This fact favours the characterization of damage in periodic structures, as it allows attention to be focused on considerably fewer modes than the total number of physical modes of the structure. Considering this, Fig. 11 furnishes the frequency decays of the first solution of the first (Fig. 11(a)) and second

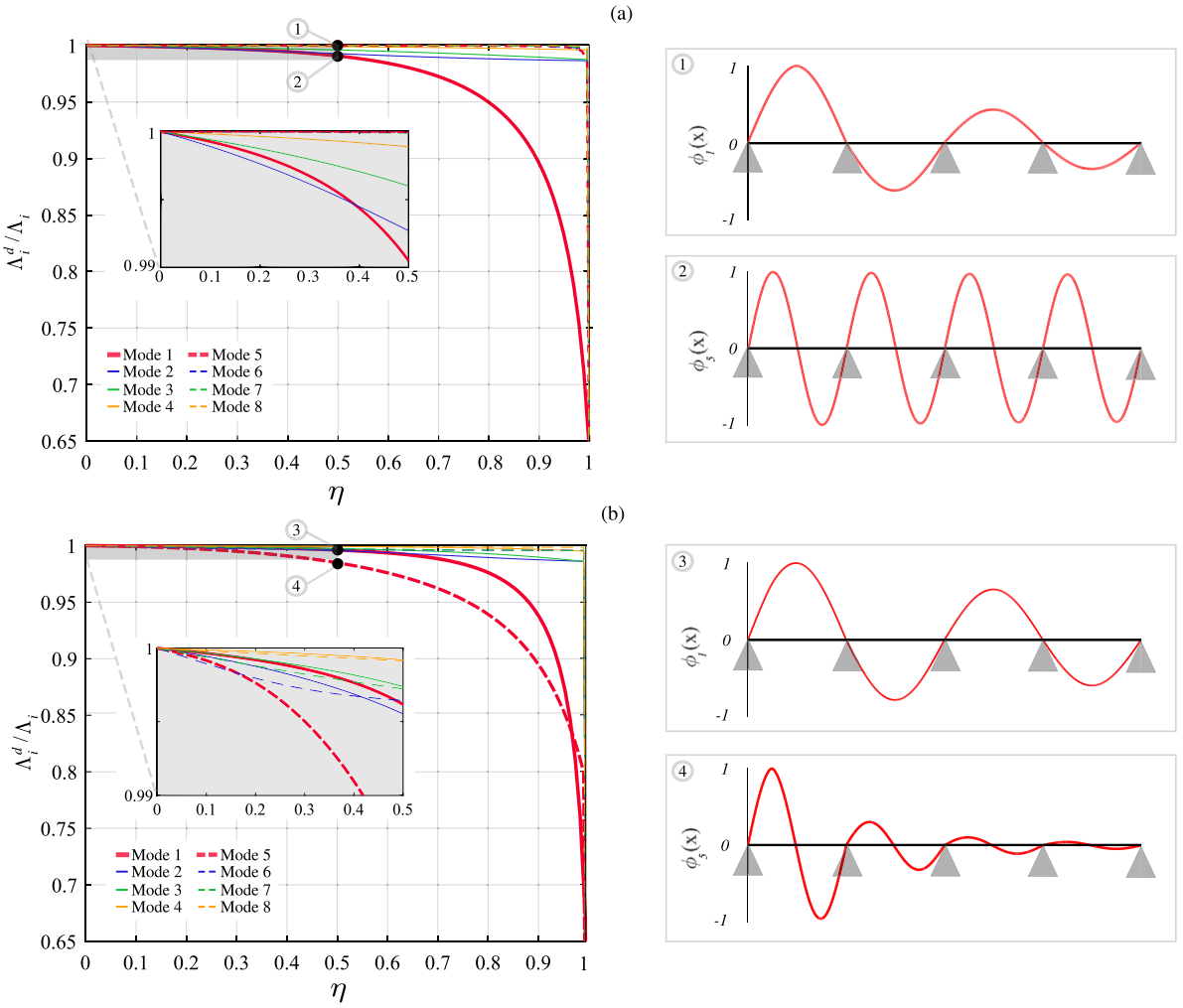

Fig. 10. Abacuses of damage-induced decays in the first (Modes 1-4) and second (Modes 5-8) modal order resonant frequencies of a 4-spans bridge ($\beta L = 1$) versus the intensity of one single defect η with a fixed extension $\zeta = 0.05$ in the first span $S = 1$ at positions $\chi = 0.5$ (a) and $\chi = 0.25$ (b). Frequency decays are presented in non-dimensional form as Λ_i^d/Λ_i, $i = 1, \ldots, 8$, with superscript "d" denoting the damage condition.

(Fig. 11(b)) modal order resonant frequencies of a 4 spans bridge with connection degree $\beta L = 1$ induced by one single defect with extension $\zeta = 0.05$ and located at different positions χ across all the spans of the bridge. In this figure, each line represents a different damage severity level η.

In light of these results and the previous analyses, it can be stated that the left branch of the envelopes of the roots of the characteristic equation can be used as an effective damage-sensitive feature. The reported analyses have shown that this branch can be approximated by the isostatic configuration ($\beta L = 0$). Therefore, the presented investigation advocates the implementation of the global OMA of multi-span bridges for damage detection purposes, by tracking at least the mode presenting the lowest frequency in each modal order. Such an approach may also trivially provide information on the damage localization at a span level. Instead, a more accurate damage localization would require the inverse calibration of a continuous model, for which the presented analytical model may serve as a flexible and low resource-intensive solution.

3.3. Real case application: the Trigno V Bridge

The Trigno V Bridge is a seven-spans highway concrete-girder bridge located in the Italian region of Abruzos, between the municipalities of Isernia and San Salvo. The viaduct is 11.5 m wide, and all the spans present equal length of 33.7 m (see Fig. 12(a)). The bridge cross-section is composed by three I-shaped pre-stressed girders separated by 3.8 m between axes and connected to a 0.25 m thick reinforced concrete deck with transverse tie diaphragms spaced every 11.2 m. The main geometrical and mechanical properties of the viaduct to be used in the subsequent modelling are reported in Table 2. On October 13th 2021, an ambient vibration test (AVT) was conducted to characterize the dynamic behaviour of the viaduct. The monitoring system comprised 50 MEMS

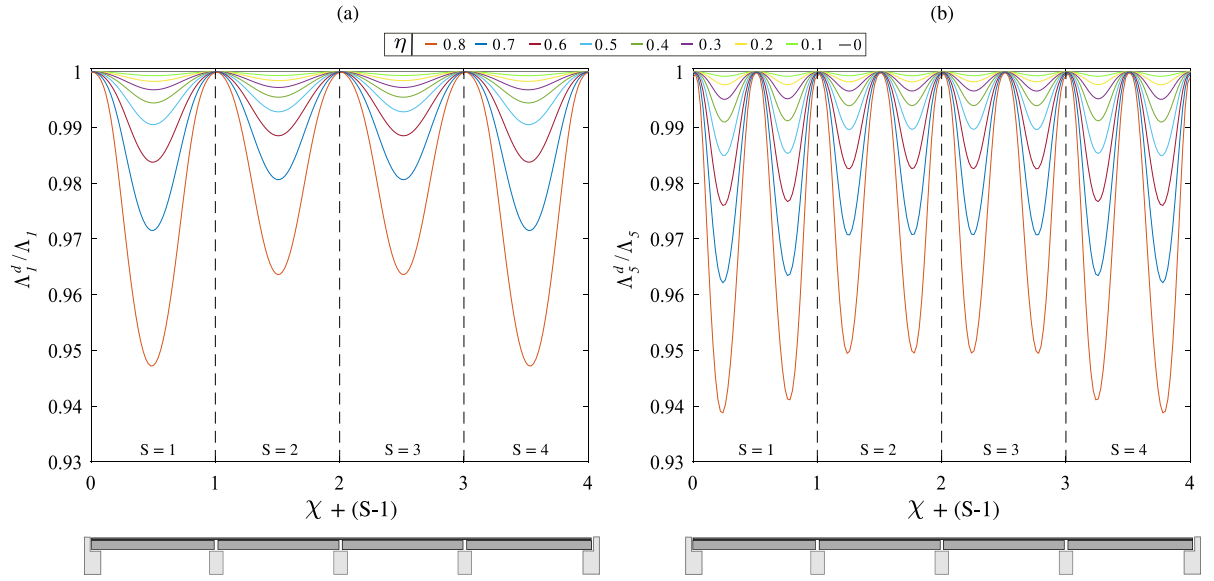

Fig. 11. Abacuses of damage-induced decays in the first solution of the first (a) and second (b) modal order resonant frequencies of a 4-spans bridge ($\beta L = 1$) versus the position of one single defect χ with a fixed extension $\zeta = 0.05$ and increasing damage intensities η. Frequency decays are presented in non-dimensional form as Λ_i^d/Λ_i, $i = 1, 5$, with superscript "d" denoting the damage condition.

Table 2
Geometrical and mechanical parameters used for the modelling of the Trigno V Bridge.

Geometrical parameters			Mechanical parameters		
L	33.7 m	Span length	ρ	2500 kg/m^3	Mass density of concrete
A	5.0838 m^2	Cross-section area	$E = E_d$	35 GPa	Concrete elastic modulus
I	2.6408 m^4	Cross-section inertia	$I_{d,cr}$	0.0619 m^4	Cracked link deck inertia
t_d	0.25 m	Deck thickness			

accelerometers (±2 g, 24-bit ADC, noise density 22.5 μg/$\sqrt{}$ Hz) distributed along the entire structure, resulting in 81 measurement channels. Each span was equipped with 4 uniaxial accelerometers in the z-direction, one biaxial accelerometer in the y- and z-directions, and one triaxial accelerometer. Additionally, the piles were instrumented with a biaxial accelerometer in the x- and y-directions at the top of each of the six piles, and a triaxial accelerometer at the base of the first and last piles. However, for the purpose of this research, only the vertical channels deployed on the deck are investigated, whose layout is depicted in Fig. 12(b). This arrangement comprises 6 channels per span located at the quarter and mid-span positions on the two sides of the deck, which amounts to a total of 42 channels. Four 30 min long acquisitions were conducted at a sampling rate of 200 Hz and used in this study to illustrate the potential of the formulation previously introduced in Section 3.1.1 to automate the definition of the identification parameters in SSI algorithms (i.e. cut-off threshold in the Hierarchical Clustering, maximum and minimum model orders, time lag, tolerances). It is important to remark that the scope of this work is limited to the automated identification of modal characteristics through AVT for their subsequent use as reference baseline in continuous OMA and modal tracking applications. Although the implementation of the proposed methodology to dynamically tune the SSI parameters in continuous monitoring applications may be straightforward, new methodological challenges will surely arise in that case, such as the appearance of environmental effects upon the inter-span coupling conditions. Therefore, this aspect is left for future work.

The acceleration records were processed through a simple filtering sequence involving the elimination of linear trends and decimation to a sampling frequency f_s of 100 Hz. The filtered acceleration time series were used to conduct OMA through the automated Covariance-driven SSI method (Cov-SSI) implemented in the P3P software [39]. The Cov-SSI method is controlled by two user-defined hyperparameters, including the model order and the maximum investigated time-lag τ among the measurements. The latter determines the dimensions of the Toeplitz matrix of covariances ($\mathbf{T}_{1|_{j_b}} \in \mathbb{R}^{lj_b \times lj_b}$, l being the number of measuring channels) through the relationship $\tau = (2j_b - 1)\frac{1}{f_s}$ [39]. Too small values of j_b may cause the algorithm to fail at finding low-frequency modes, while too large values increase the number of spurious modes and raise the computational burden of the identification. In common practice, the time-lag parameter j_b is usually set up according to a certain rule-of-thumb such as the one proposed by Reynders et al. [51] as:

$$j_b > 10\frac{f_s}{2f_o}, \tag{20}$$

where f_o stands for the minimum expectable resonant frequency of interest. Given the geometric/mechanical properties in Table 2, the theoretical fundamental frequency for the isostatic configuration ($\Lambda = \pi$) can be extracted from Eq. (11) as $f_o = 3.72$ Hz. In

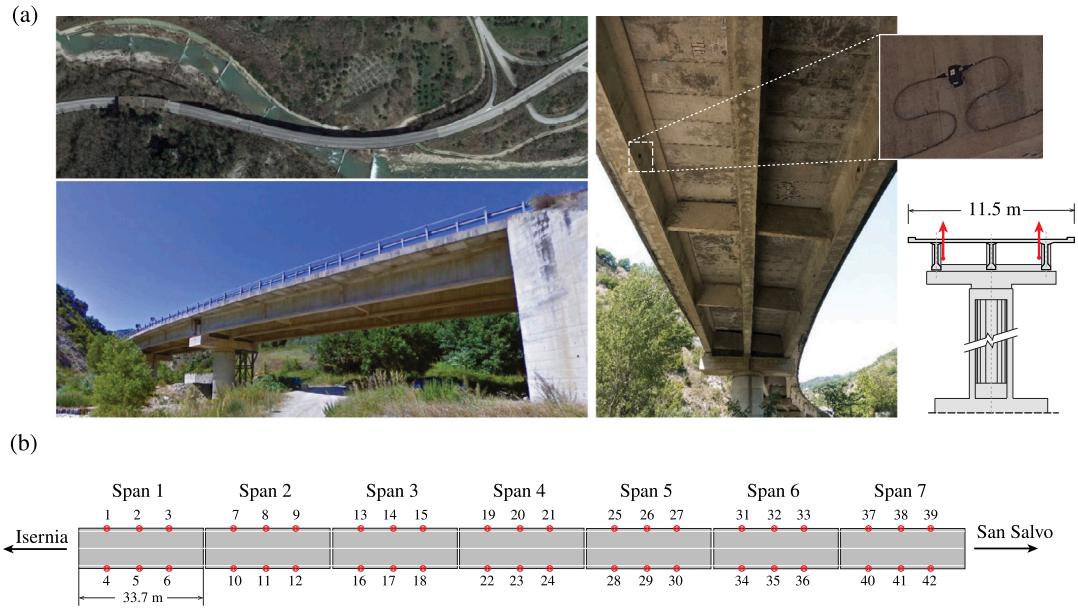

Fig. 12. Geometry of the Trigno V Bridge (a) and position of the accelerometers in vertical direction (b).

this light, the time lag in the Cov-SSI method was fixed to 3.59 s ($j_b = 180$) in all the analyses. Instead, the model order was varied depending on the number of spans considered in the analysis. To do so, the maximum model order was tailored through the visual inspection of the Shannon entropy of the singular values of the Toeplitz matrix as proposed in [52]. Specifically, the maximum model order was selected for each identification as the model order in which a sudden decrease of the singular entropy variation is observed. On this basis, the maximum order was set to 120 when analysing a number of spans less than or equal to 4, and increased to 200 when considering 5 to 7 spans. A minimum model order of 2 was defined in all the analyses, and the complete range of orders was explored with steps of 2. By means of stabilization diagrams, the elimination of spurious poles was performed by prescribing a set of Hard Criteria (HC), including modal phase collinearity (MPC) and mode phase deviation (MPD). MPC evaluates the linear relationship between the real and imaginary part of the modal components, while MPD estimates the statistical variation of the phase angles of each modal component [34]. Both parameters are dimensionless and range from 0 to 1. In classically damped structures, the corresponding mode shapes are real-valued (aligned modal components in the complex plane) with MPC and MPD metrics approaching the ideal values of 1 and 0, respectively. Non-classically damped systems or insufficiently excited modes of vibration tend to exhibit highly complex modes with MPC/MPD metrics far from these ideal limits. In practice, lightly damped civil engineering structures tend to exhibit real normal modes, thereby MPC and MPD indicators are often used to filter out complex mode shapes that are commonly associated with noise or spurious modes. Therefore, the HC considered in the identification included the elimination of system poles with negative or unrealistically high damping rates ($\xi \leq 10\%$), mode phase deviation values ($MPD \leq 50\%$), and mode phase collinearity factors ($MPC \geq 50\%$). Afterwards, stable poles across the considered model orders were identified by imposing a set of Soft Criteria between every pair of poles i and j identified at model orders m and $m-1$, including maximum relative differences in terms of resonant frequencies $(f_i^m - f_j^{m-1})/f_i^m < 1\%$, damping ratios $(\xi_i^m - \xi_j^{m-1})/\xi_i^m < 5\%$, and MAC values $MAC(\boldsymbol{\phi}_i^m, \boldsymbol{\phi}_j^{m-1}) \geq 0.99$. Finally, the identified ensemble of stable poles was used to extract the physical modes through hierarchical clustering.

Firstly, the identification of the viaduct was conducted by processing subgroups of channels belonging to one span at a time assuming perfectly isostatic conditions. In these analyses, according to Eq. (16) the cut-off distance threshold $\overline{d}$ in the hierarchical clustering was set to 0.07 after some manual tuning. As a sample of the conducted identifications, Fig. 13 shows the stabilization diagram derived from the analysis of the first span. The identification results in this figure reveal the existence of seven alignments of stable poles in the frequency range up to 40 Hz. Note that the two first clusters (Cl-1 and Cl-2, with average frequencies of 3.89 and 4.17 Hz) are aligned with two marked peaks in the singular values (SVs) of the spectral matrix of accelerations (inserted in the background of Fig. 13 for clarity purposes). Indeed, these clusters are densely populated with stable poles identified at most of the considered model orders. Conversely, the remaining clusters in the frequency broadband between 10 and 35 Hz are more sparsely populated, with a considerable number of misclassifications at several model orders. These results agree with the inspection of the SVs, which, despite exhibiting considerably energy concentrations at frequencies neighbouring the identified clusters (particularly Cl-3 to Cl-5), do not present clear resonant peaks. This is conceivably ascribed to the interaction with the traffic, which was considerable intense during the acquisitions and may be masking the structural vibrations in this frequency range or, alternatively, maybe more intensively exciting the first-order modes. Another reasonable explanation is related to the fact that the wavelength of higher-order modes is shorter, implying that the modes are more localized and therefore more difficult to identify from measurements on a

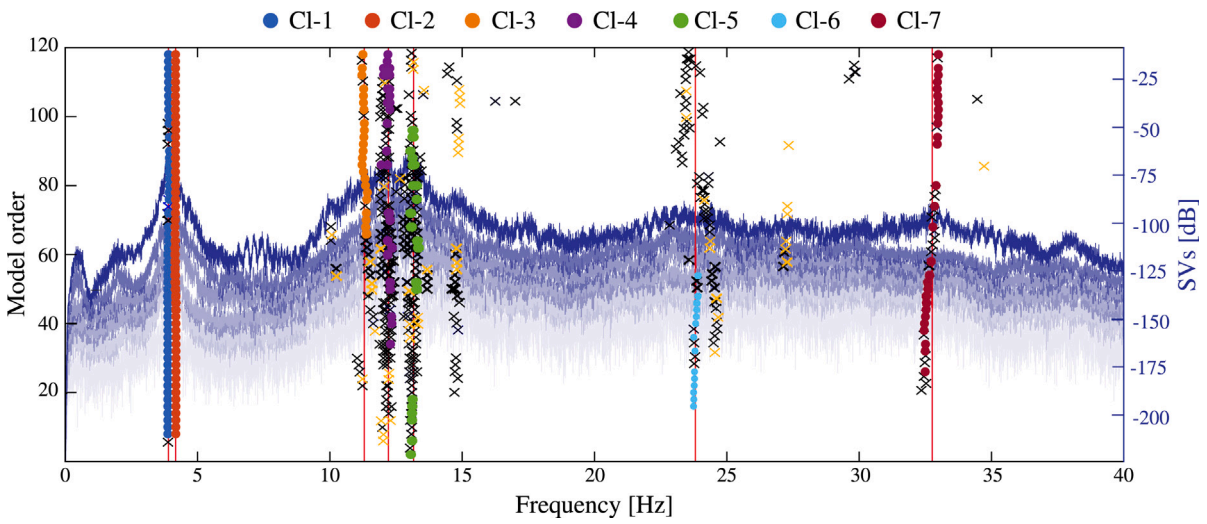

Fig. 13. Clustering results obtained for the first span of the Trigno V Bridge. Yellow and black crosses stand for unclustered stable and unstable poles. (For interpretation of the references to colour in this figure legend, the reader is referred to the web version of this article.)

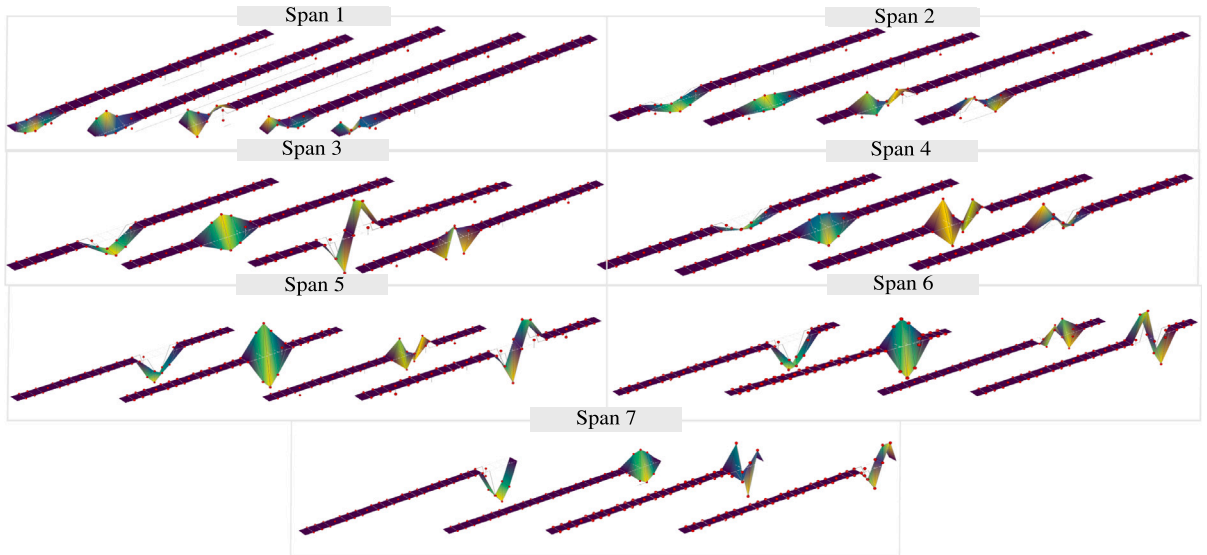

Fig. 14. Experimentally identified natural mode-shapes of the Trigno V bridge when conducting span-wise OMA.

single span. Similar modal localization issues are typical for structures that are not perfectly periodic, but for which there are small differences between the spans. Following a similar procedure and after the interpretation of the natural mode shapes, four to five vibration modes have been successfully identified in all the spans as reported in Table 3. Note that the properties of the modes reported in this table have been extracted from the centroids of the identified clusters of poles. These comprise two closely spaced modes, namely a first-order flexural mode (3.83–3.89 Hz) and a first-order torsional mode (4.00–4.17 Hz), a second-order torsional mode (9.85–12.13 Hz), a second-order flexural mode (12.05–13.16 Hz) and, finally, a third-order torsional mode (32.76–33.50 Hz). The corresponding mode shapes are depicted in Fig. 14. Note that all the spans exhibit very close resonant frequencies (especially the first two modes with maximum relative differences of 2.60 and 4.08%, respectively) and mode shapes with very similar wavelengths. Only larger frequencies are found for the end spans 1 and 7, which may be ascribed to the presence of local effects due to the connection between the bridge, abutments and the remaining road.

Secondly, the dynamic identification is conducted by incorporating one span at a time until covering the whole viaduct, starting with the first span. The experimental identification results were compared against the predictions of the analytical model previously introduced in Section 2. To do so, the inter-span rotational stiffness was estimated from Eq. (18) and considering the geometrical/mechanical properties from Table 2, obtaining a value of k = 1.287E+9 Nm (βL = 0.469). Specifically, the moment of inertia of the cracked section $I_{d,cr}$ was evaluated considering the position of the neutral axis in the cracked stage. The resulting

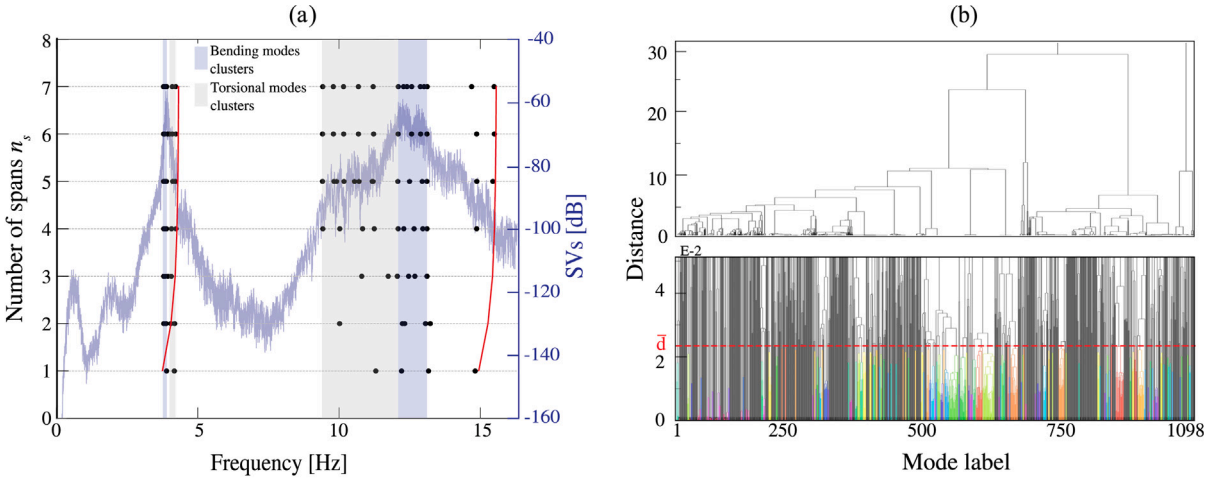

Fig. 15. Modal identification of the Trigno V bridge (11:00 p.m., October 13th 2021) as the number of spans increases (a), and detailed view of the hierarchical clustering dendogram with the optimal cut-off distance $\bar{d}$ (b). (For interpretation of the references to colour in this figure legend, the reader is referred to the web version of this article.)

Table 3
Results of the span-wise modal identification of the Trigno V Bridge (11:00 p.m., October 13th 2021).

Span	1st bending mode		1st torsional mode		2nd torsional mode		2nd bending mode		3rd torsional mode	
	f_i [Hz]	ξ_i [%]	f_i [Hz]	ξ_i [%]	f_i [Hz]	ξ_i [%]	f_i [Hz]	ξ_i [%]	f_i [Hz]	ξ_i [%]
1	3.89	5.78	4.17	6.46	11.30	4.40	13.16	2.94	32.76	3.27
2	3.79	5.58	4.06	5.25	9.85	6.14	12.32	1.86	–	–
3	3.84	5.80	4.06	6.14	–	–	12.67	3.32	33.50	2.24
4	3.85	5.56	4.02	9.11	9.95	5.02	12.05	1.72	–	–
5	3.86	5.50	4.11	6.24	9.77	3.70	12.65	1.73	–	–
6	3.83	5.47	4.00	7.67	9.78	6.40	12.73	3.80	–	–
7	3.89	5.70	4.11	7.72	12.13	2.44	13.13	2.89	–	-

theoretical envelopes of the first and second order flexural poles of the viaduct are depicted in Fig. 15(a) with red solid lines. For the experimental identification, the cut-off distance threshold $\bar{d}$ for the hierarchical clustering of stable poles was defined as 0.07 when identifying up to 3 spans. Instead, when considering more than 3 spans, the cut-off distance threshold was estimated from Eq. (17) by analysing the roots of the characteristic matrix of the analytical model. The centroids of the experimentally identified modal clusters are plotted in Fig. 15 with black scatter points. It is important to remark that the comparison between the experimental and theoretical results is not completely rigorous, since the OMA is conducted over subsets of channels belonging to consecutive spans while the analytical model simulates the connection of an increasing number of spans. Nonetheless, the close correlation in Fig. 15 between the experimental poles and the theoretical envelope of the first order bending modes supports the accuracy of the proposed formulation. Conversely, the correlation is not so clear for the second order bending modes. Indeed, an appreciable gap can be noted between the theoretical envelope and the experimental poles, with considerably lower frequency values in the latter. These differences are conceivably due to limitations in the adopted Euler–Bernoulli formulation and to the mode shapes localization at higher frequencies, as discussed previously. In particular, the formulation disregards any bending–torsion interaction effects, the vertical stiffness of the piers, as well as local characteristics of the bridge including the transverse diaphragms. To achieve closer fittings between experimental and theoretical modes, a detailed 3D FEM of the viaduct is most probably required. Indeed, as reported hereafter, the experimentally identified poles in the frequency broadband between 12 Hz and 15 Hz exhibit clear evidence of bending-torsion coupling effects as well as vertical motions at the piers.

Finally, the effectiveness of the developed analytical model to assist the global AOMA of the Trigno V Bridge is investigated. To do so, all the acceleration channels are included simultaneously in the Cov-SSI, and the optimal model-based cut-off distance previously proposed in Section 3.1.1 is used in the hierarchical clustering phase. Considering the inter-span rotational stiffness k = 1.287E+9 Nm estimated above, the cut-off threshold $\bar{d}$ can be computed through Eq. (16) among the roots of the characteristic matrix (n_s = 7) corresponding to first order bending modes. By substituting the values in Table 5 in Eq. (17), the cut-off distance threshold is estimated as $\bar{d}$ = 2.348E-2 and then used to cut the dendogram resulting from the hierarchical clustering algorithm as reported in Fig. 15(b). The resulting stabilization diagram with the physical clusters identified through the global AOMA of the Trigno V Bridge is shown in Fig. 16. A total of 22 clusters were identified, most of them forming dense groups of poles in the frequency ranges 3.788–3.895 Hz (first order bending), 4.100–4.220 Hz (first order torsion), 9.421–11.206 Hz (second order torsion), and 12.096–13.117 Hz (second order torsion). The corresponding resonant frequencies f_i, damping ratios ξ_i, and cluster sizes Cl_i^s are reported in Table 4, and the mode shapes are furnished in Fig. 17. Note that the MAC matrix shown in this figure is almost perfectly diagonal with most

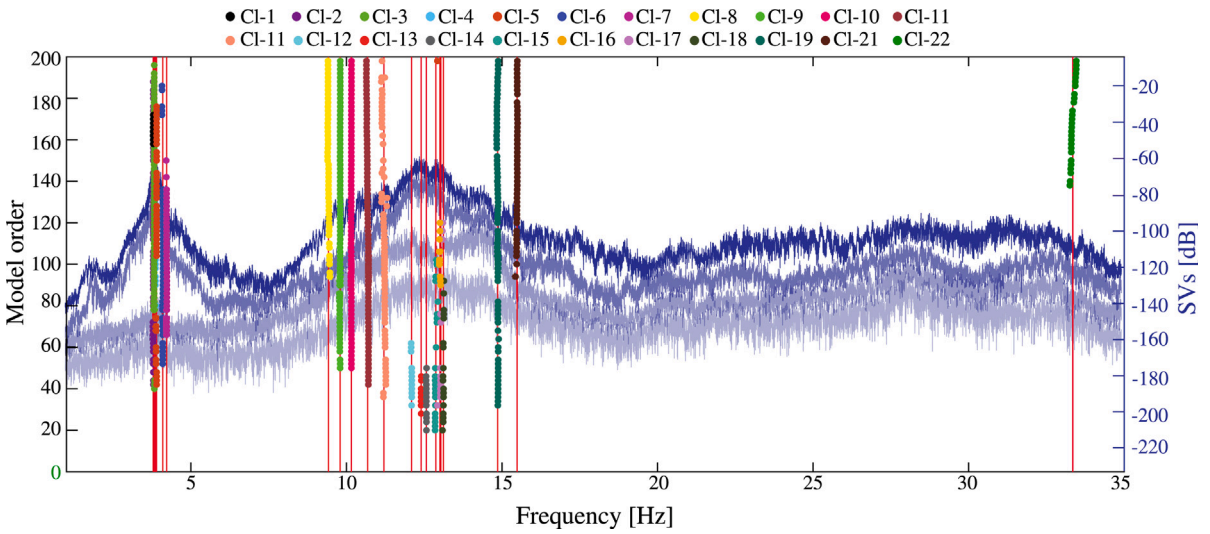

Fig. 16. Global OMA of the Trigno V Bridge (11:00 p.m., October 13th 2021).

Table 4
Results of the global modal identification of the Trigno V Bridge (11:00 p.m., October 13th 2021). The term Cl_i^s denotes the number of poles (size) populating the clusters, respectively.

Mode	f_i [Hz]	ξ_i [%]	Cl_i^s	Mode	f_i [Hz]	ξ_i [%]	Cl_i^s	Mode no.	f_i [Hz]	ξ_i [%]	Cl_i^s	Mode	f_i [Hz]	ξ_i [%]	Cl_i^s
1	3.788	7.69	8	7	4.220	6.02	35	13	12.096	2.73	11	19	13.117	3.27	18
2	3.791	5.67	57	8	9.421	5.39	47	14	12.402	2.84	8	20	14.861	3.08	73
3	3.818	5.70	61	9	9.796	3.80	73	15	12.569	3.08	13	21	15.487	3.34	44
4	3.860	5.91	16	10	10.157	3.61	75	16	12.868	2.79	20	22	33.350	2.43	26
5	3.895	6.20	45	11	10.683	3.70	78	17	13.005	1.84	7				
6	4.100	5.46	35	12	11.206	3.41	63	18	13.024	3.72	7				

Table 5
Non-dimensional frequency Λ of $\det(\Gamma_{7-1}) = 0$ and frequencies f of the first order bending modes of the Trigno V bridge.

Mode no.	1	2	3	4	5	6	7
Λ_i	π	3.1543	3.1894	3.2392	3.2934	3.3413	3.3741
$f_{1,i}^t$	3.7299	3.7601	3.8443	3.9653	4.0991	4.2192	4.3023

off-diagonal terms close to zero, which is an indication of the quality of the identification. Only some correlation is observed between Modes 16 and 17 with a MAC value of 0.6. Nonetheless, given their considerable difference in terms of frequency, we assume that these modes are certainly different physical modes and this MAC value arises due to a limitation of the spatial discretization of the mode shapes. After the interpretation of the mode shapes in this figure, one can conclude that: Modes 1 to 5 correspond to first order bending modes; Modes 6 to 12 are first order torsional modes; Modes 13 to 19 are second order bending modes; Mode 20 is a mixed bending-torsional mode; Modes 21 and 22 represent second order torsional modes. Some of these modes exhibit a significant localization of the modal components in some spans instead of others. As mentioned in the previous paragraph, this behaviour may be partly attributed to the non-perfect periodicity of the structure, resulting from slight variations in the structural characteristics of the spans, such as differences in their length and stiffness. Another plausible explanation is related to the existence of limited inter-span rotational coupling, which is consistent with the low value of the parameter βL obtained through the proposed formulation. It is also important to highlight the appearance of certain bending-torsion interactions and vertical motions in the cross-sections of the piers in Modes 13 to 19. Such effects, disregarded by the developed analytical model, conceivably contribute to explain the poor fitting of the second-order bending modes as previously reported in Fig. 15.

Based on the results of the operational modal identification of the Trigno V Bridge, it is concluded that among the identified modes, those of greatest relevance in the stage of damage assessment are those presenting the lowest frequency within the clusters belonging to each modal order. To this purpose, attention should be focused on modes 1, 6, 8 and 13 in Fig. 17. Comparing Tables 3 and 4, it can be also noted that carrying out a spanwise OMA may result in missing the lowest frequencies within the same cluster of modes, therefore missing identification of the most damage sensitive modes. This discordance may be due to localization effects due to deviations from the periodicity, as previously discussed, and suggests to take extra care when adopting SHM strategies based on spanwise OMA results. In such cases, a single global OMA analysis is always recommended to check the accuracy and tune the spanwise identification.

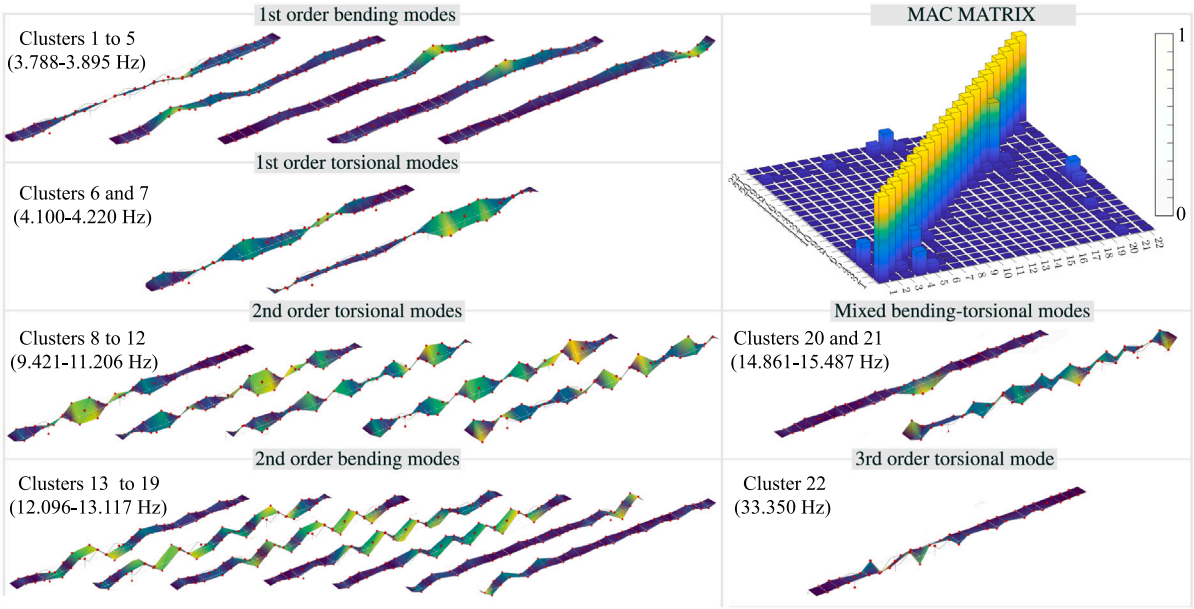

Fig. 17. Global mode-shapes of the Trigno V bridge in ascending order (11:00 p.m., October 13th 2021) and corresponding MAC matrix.

4. Conclusions

This paper has presented an analytical model to assist the AOMA of quasi-periodic multi-span partially continuous bridges. The formulation is based on the closed-form resolution of the free vibration problem of partially-continuous multi-span Euler–Bernoulli beams. The inter-span coupling, defined through rotational springs, allows correlating different degrees of rotational continuity with the bending resonant frequencies of multi-span bridges. On this basis, the developed formulation has been used to define the optimal distance threshold to be used in the hierarchical clustering of stable poles determined through SSI and stabilization diagrams. In the proposed methodology, the optimal distance has been therefore employed to cut the dendogram generated through the unsupervised machine learning hierarchical clustering algorithm and infer the modal features of the structure. The optimal cut-off distance is estimated through a two-steps procedure: (i) estimation of the inter-span rotational coupling through the mechanical characteristics of the connection between spans; (ii) computation of the average distance between every two consecutive frequencies of the first order bending mode to define the cut-off distance threshold. The effectiveness of the proposed methodology has been appraised through detailed parametric analyses and through a real-world in-operation case study, the Trigno V Bridge. Overall, the presented research extends the OMA-related knowledge on quasi-periodic multi-span bridges. One aspect of potential improvement for the developed mechanics model is the incorporation of torsional degrees of freedom to account for possible bending/torsional interaction effects. While such an extension is left for future work, the presented approach already meets the main goal of this study: the development of an easily implementable mechanics-based approach for optimally selecting the threshold parameter to be used in the Hierarchical Clustering phase of automated SSI. The significance of the proposed results stems from the vast presence of this kind of bridges all over the world, for which the proposed formulation may represent a versatile and computationally-efficient approach for tailoring AOMA applications. The key findings of this work can be listed as follows:

- The presented results and discussion have pinpointed that the capability of OMA to identify all the global modes of multi-span bridges is closely related to the structural features of the structure under investigation. These include the number of spans, regularity in the mechanical/geometrical properties across the spans, and the inter-span coupling conditions. In particular, the gap between the resonant frequencies of a certain mode order depends upon the connection degree between the spans and the number of spans.
- The reported parametric analyses have demonstrated that the damage-induced effects upon the resonant frequencies of multi-span bridges vary considerably according to the damage position, intensity and extension. Interestingly, it has been shown that local defects lead to frequency decays that, in some cases, can even be concentrated in one bending mode order, while the effects of spread damage distribute across several mode orders. Furthermore, parametric analyses show that the mode whose damage-induced decay is most pronounced is the first one belonging to each modal order. This fact allows attention to be focused on fewer modes in the calibration phase through iterative model updating and represents a clear advantage in the field of damage assessment of periodic structures.
- Global OMA is needed to conduct precise damage localization, while span-wise OMA may suffice to detect the appearance of damage but may be inconsistent in the determination of which span is damaged. In fact, one may confuse global and

local modes since one span may be affected by a damage located in a different span. Nevertheless, the span-wise analysis is not considered unsuitable for damage identification, but the implementation of such an analysis methodology requires a subsequent research step. Indeed, the possibility to track damages starting from the results of a span-wise OMA is extremely advantageous since physical mode-shapes and frequencies can be more easily inferred when spans are separately analysed. However, a global analysis is always recommended to check the accuracy and tune the spanwise identification, particularly to avoid that the most damage sensitive modes are missed in the identification.

Declaration of competing interest

The authors declare that they have no known competing financial interests or personal relationships that could have appeared to influence the work reported in this paper.

Data availability

Data will be made available on request.

Acknowledgements

The financial support and access to the monitoring data of the Trigno Bridge by Anas S.p.A are gratefully acknowledged. E. Tomassini was supported by University of Perugia, Italy through the funded project "Math4Bridges-Machine Learning and Transfer Learning Approaches for Structural Health Monitoring and Risk Assessment of Bridges" (MAT421FU) within the program "Fondo Ricerca di base di Ateneo, edizione 2020". E. García-Macías was supported by the Spanish Ministry of Science and Innovation through the research project "BRIDGEXT - Life-extension of ageing bridges: Towards a long-term sustainable Structural Health Monitoring" (Ref. PID2020-116644RB-I00). E. Reynders was partially supported by the Research Foundation – Flanders (FWO), research project G.0052.20N and by Flanders Innovation & Entrepreneurship, COOCK Project HBC.2019.2505.

Appendix. Derivation process of the theoretical formulation

Combining the boundary condition $\phi_i(0) = 0$ in Table 1 for the i-th intermediate span and Eq. (4) results:

$$E_i = -C_i. \tag{A.1}$$

Hence, Eq. (4) and its first and second order derivatives can be expressed as follows:

$$\phi_i(x_i) = C_i\left[\cos\left(\alpha x_i\right) - \cosh\left(\alpha x_i\right)\right] + D_i \sin\left(\alpha x_i\right) + F_i \sinh\left(\alpha x_i\right), \tag{A.2}$$

$$\phi_i'(x_i) = -C_i\alpha\left[\sin\left(\alpha x_i\right) + \sinh\left(\alpha x_i\right)\right] + D_i\alpha\cos\left(\alpha x_i\right) + F_i\alpha\cosh\left(\alpha x_i\right), \tag{A.3}$$

$$\phi_i''(x_i) = -C_i\alpha^2\left[\cos\left(\alpha x_i\right) + \cosh\left(\alpha x_i\right)\right] - D_i\alpha^2\sin\left(\alpha x_i\right) + F_i\alpha^2\sinh\left(\alpha x_i\right). \tag{A.4}$$

The boundary conditions $\phi_i(L_i) = 0$ and $\phi_i''(L_i) = \phi_{i+1}''(0)$ in Table 1 respectively lead to:

$$C_i\left[\cos\left(\alpha L_i\right) - \cosh\left(\alpha L_i\right)\right] + D_i \sin\left(\alpha L_i\right) + F_i \sinh\left(\alpha L_i\right) = 0, \tag{A.5}$$

$$-C_i\left[\cos\left(\alpha L_i\right) + \cosh\left(\alpha L_i\right)\right] - D_i \sin\left(\alpha L_i\right) + F_i \sinh\left(\alpha L_i\right) = -2C_{i+1}. \tag{A.6}$$

The integration constants D_i and F_i can be derived by adding and subtracting Eqs. (A.5) as:

$$D_i = \frac{C_{i+1} - C_i\cos\left(\alpha L_i\right)}{\sin\left(\alpha L_i\right)}, \quad F_i = \frac{-C_{i+1} + C_i\cosh\left(\alpha L_i\right)}{\sinh\left(\alpha L_i\right)}. \tag{A.7}$$

The boundary condition $\phi_i''(L_i) = \beta_i\left[\phi_{i+1}'(0) - \phi_i''(L_i)\right]$ in Table 1 reads:

$$D_{i+1} + F_{i+1} - C_i\psi_i + C_{i+1}\varphi_i = -2\frac{\alpha}{\beta}C_{i+1}, \tag{A.8}$$

where the coefficients ψ_i and φ_i are:

$$\varphi_i = \coth\left(\alpha L_i\right) - \cot\left(\alpha L_i\right), \quad \psi_i = \operatorname{csch}\left(\alpha L_i\right) - \csc\left(\alpha L_i\right). \tag{A.9}$$

The following equation results from the replacement of the integration coefficients D_i and F_i in Eq. (A.8):

$$C_i\left(-\psi_i\right) + C_{i+1}\left(\varphi_i + \varphi_{i+1} + 2\frac{\alpha}{\beta_i}\right) - C_{i+2}\psi_{i+1} = 0. \tag{A.10}$$

The condensed matrix form of Eq. (A.10) for $i = 1, \ldots, n_s - 1$ is given in Eq. (5).

References

[1] F.Y. Xu, M.J. Zhang, L. Wang, J.R. Zhang, Recent highway bridge collapses in China: review and discussion, J. Perform. Constr. Facil. 30 (5) (2016) 04016030.
[2] G.M. Calvi, M. Moratti, G.J. O'Reilly, N. Scattarreggia, R. Monteiro, D. Malomo, P.M. Calvi, R. Pinho, Once upon a time in Italy: The tale of the Morandi bridge, Struct. Eng. Int. 29 (2) (2019) 198–217.
[3] L. Gallin, Genoa bridge collapse to cost insurers up to $685 million: J.P. Morgan, 2018, Reinsurance News.
[4] American Society of Civil Engineers ASCE, 2021 Report card for America's infrastructures, 2021.
[5] G. Zhang, Y. Liu, J. Liu, S. Lan, J. Yang, Causes and statistical characteristics of bridge failures: A review, J. Traffic Transp. Eng. (English Edition) 9 (3) (2022) 388–406.
[6] J. Tan, K. Elbaz, Z. Wang, J. Shen, J. Chen, Lessons learnt from bridge collapse: A view of sustainable management., Sustainability 12 (3) (2020) 1205.
[7] G.D. Zhou, T.H. Yi, W.J. Li, J.W. Zhong, G.H. Zhang, Standardization construction and development trend of bridge health monitoring systems in China, Adv. Bridge Eng. 1 (1) (2020) 1–18.
[8] Federal Highway Administration (FHWA) of U.S. Department of Transportation, Apportionment of highway infrastructure program funds pursuant to the department of transportation appropriations act, 2022, 2022.
[9] K. Gkoumas, F. Marques Dos Santos, M. Van Balen, A. Tsakalidis, A. Ortega Hortelano, M. Grosso, A. Haq, F. Pekar, Research and innovation in bridge maintenance, inspection and monitoring, Publ. Off. Eur. Union (2019).
[10] Italian Ministry of Infrastructure and Transport, Guidelines on risk classification and management, safety assessment and monitoring of existing bridges, 2022.
[11] M. Torti, S. Sacconi, I. Venanzi, F. Ubertini, Monitoring-informed life-cycle cost analysis of deteriorating RC bridges under repeated earthquake loading, J. Struct. Eng. (United States) 148 (9) (2022).
[12] E. Reynders, System identification methods for (operational) modal analysis: Review and comparison, Arch. Comput. Methods Eng. 19 (2012) 51–124.
[13] E. García-Macías, F. Ubertini, Integrated SHM systems: Damage detection through unsupervised learning and data fusion, in: Structural Health Monitoring Based on Data Science Techniques, Springer, 2022, pp. 247–268.
[14] R. Brincker, C. Ventura, Introduction to Operational Modal Analysis, Wibley, 2015.
[15] R. Hou, Y. Xia, Review on the new development of vibration-based damage identification for civil engineering structures: 2010–2019, J. Sound Vib. 491 (2021) 115741.
[16] P. Kaewniam, M. Cao, N.F. Alkayem, D. Li, E. Manoach, Recent advances in damage detection of wind turbine blades: A state-of-the-art review, Renew. Sustain. Energy Rev. 167 (2022) 112723.
[17] Q. Sun, W. Yan, W. Ren, L. Liu, Application of transmissibility measurements to operational modal analysis of railway, highway, and pedestrian cable-stayed bridges, Measurement 148 (2019) 106880.
[18] K. Maes, L. Van Meerbeeck, E. Reynders, G. Lombaert, Validation of vibration-based structural health monitoring on retrofitted railway bridge KW51, Mech. Syst. Signal Process. 165 (2022).
[19] Á. Cunha, E. Caetano, F. Magalhães, C. Moutinho, Dynamic identification and continuous dynamic monitoring of bridges: different applications along bridges life cycle, Struct. Infrastruct. Eng. 14 (4) (2018) 445–467.
[20] V. Gattulli, A. Cunha, E. Caetano, F. Potenza, A. Arena, U. Di Sabatino, Dynamical models of a suspension bridge driven by vibration data, Smart Struct. Syst. 27 (2) (2021) 139–156.
[21] E. García-Macías, F. Ubertini, Real-time Bayesian damage identification enabled by sparse PCE-Kriging meta-modelling for continuous SHM of large-scale civil engineering structures, J. Build. Eng. 59 (2022) 105004.
[22] A. Fernandez-Navamuel, D. Zamora-Sánchez, Á.J. Omella, D. Pardo, D. Garcia-Sanchez, F. Magalhães, Supervised deep learning with finite element simulations for damage identification in bridges, Eng. Struct. 257 (2022) 114016.
[23] J. Shu, C. Zhang, Y. Gao, Y. Niu, A multi-task learning-based automatic blind identification procedure for operational modal analysis, Mech. Syst. Signal Process. 187 (2023) 109959.
[24] P. Gardner, L. Bull, J. Gosliga, J. Poole, N. Dervilis, K. Worden, A population-based SHM methodology for heterogeneous structures: Transferring damage localisation knowledge between different aircraft wings, Mech. Syst. Signal Process. 172 (2022) 108918.
[25] B. Peeters, G. De Roeck, Reference-based stochastic subspace identification for output-only modal analysis, Mech. Syst. Signal Process. 13 (6) (1999) 855–878.
[26] C. Rainieri, G. Fabbrocino, E. Cosenza, Automated Operational Modal Analysis as structural health monitoring tool: theoretical and applicative aspects, in: Key Engineering Materials, Vol. 347, Trans Tech Publ, 2007, pp. 479–484.
[27] F. Magalhães, Á. Cunha, Explaining operational modal analysis with data from an arch bridge, Mech. Syst. Signal Process. 25 (5) (2011) 1431–1450.
[28] E. Reynders, J. Houbrechts, G. De Roeck, Automated interpretation of stabilization diagrams, in: Modal Analysis Topics, Volume 3, Springer, 2011, pp. 189–201.
[29] F. Ubertini, C. Gentile, A.L. Materazzi, Automated modal identification in operational conditions and its application to bridges, Eng. Struct. 46 (2013) 264–278.
[30] Y. He, J.P. Yang, Y.F. Li, A three-stage automated modal identification framework for bridge parameters based on frequency uncertainty and density clustering, Eng. Struct. 255 (2022) 113891.
[31] P. Cheema, M.M. Alamdari, G. Vio, F. Zhang, C. Kim, Infinite mixture models for operational modal analysis: An automated and principled approach, J. Sound Vib. 491 (2021) 115757.
[32] J.X. Mao, H. Wang, Y.G. Fu, B.F. Spencer Jr., Automated modal identification using principal component and cluster analysis: Application to a long-span cable-stayed bridge, Struct. Control Health Monit. 26 (10) (2019) e2430.
[33] J. Franklin, The elements of statistical learning: data mining, inference and prediction, Math. Intelligencer 27 (2) (2005) 83–85.
[34] E. Reynders, J. Houbrechts, G. De Roeck, Fully automated (operational) modal analysis, Mech. Syst. Signal Process. 29 (2012) 228–250.
[35] G. Zini, M. Betti, G. Bartoli, A quality-based automated procedure for operational modal analysis, Mech. Syst. Signal Process. 164 (2022) 108173.
[36] H. Xu, W.L. Li, Dynamic behavior of multi-span bridges under moving loads with focusing on the effect of the coupling conditions between spans, J. Sound Vib. 312 (4–5) (2008) 736–753.
[37] V. De Salvo, G. Muscolino, A. Palmeri, A substructure approach tailored to the dynamic analysis of multi-span continuous beams under moving loads, J. Sound Vib. 329 (15) (2010) 3101–3120.
[38] J. Zhang, K. Maes, G. De Roeck, E. Reynders, C. Papadimitriou, G. Lombaert, Optimal sensor placement for multi-setup modal analysis of structures, J. Sound Vib. 401 (2017) 214–232.
[39] E. García-Macías, A. Ruccolo, M.A. Zanini, C. Pellegrino, C. Gentile, F. Ubertini, P. Mannella, P3P: a software suite for autonomous SHM of bridge networks, J. Civ. Struct. Health Monit. (2022) 1–18.
[40] K. Liu, E. Reynders, G. De Roeck, G. Lombaert, Experimental and numerical analysis of a composite bridge for high-speed trains, J. Sound Vib. 320 (1–2) (2009) 201–220.

[41] J. Zhang, E. Reynders, G. De Roeck, G. Lombaert, Model updating of periodic structures based on free wave characteristics, J. Sound Vib. 442 (2019) 281–307.
[42] J. Zhang, K. Maes, G. De Roeck, G. Lombaert, Model updating for a large multi-span quasi-periodic viaduct based on free wave characteristics, J. Sound Vib. 506 (2021) 116161.
[43] S.S. Rao, Vibration of Continuous Systems, John Wiley & Sons, Inc, 2019.
[44] F. Zhang, Matrix Theory: Basic Results and Techniques, Springer New York, NY, 2011.
[45] E. García-Macías, A. Martínez-Castro, Hilbert transform-based semi-analytic meta-model for maximum response envelopes in dynamics of railway bridges, J. Sound Vib. 487 (2020) 115618.
[46] R. Allemang, D. Brown, A correlation coefficient for modal vector analysis, in: Proceedings of the 1st International Modal Analysis Conference, 1982, pp. 110–116.
[47] H. Hao, Y. Xia, Vibration-based damage detection of structures by genetic algorithm, J. Comput. Civ. Eng. 16 (3) (2002) 222–229.
[48] E. Reynders, C. Van hoorickx, A. Dijckmans, Sound transmission through finite rib-stiffened and orthotropic plates, Acta Acust. United Acust. 102 (6) (2016) 999–1010.
[49] A. Au, C. Lam, J. Au, B. Tharmabala, Deck joints using debonded link slabs: Research and field tests in ontario, J. Bridge Eng. 18 (8) (2013) 768–778.
[50] D. Anastasopoulos, K. Maes, G. Lombaert, G. De Roeck, E. Reynders, Influence of frost and local stiffness variations on the strain mode shapes of a steel arch bridge, Eng. Struct. 273 (115097) (2022) 1–19.
[51] E. Reynders, G. De Roeck, Reference-based combined deterministic–stochastic subspace identification for experimental and operational modal analysis, Mech. Syst. Signal Process. 22 (3) (2008) 617–637.
[52] S. Qin, J. Kang, Q. Wang, Operational modal analysis based on subspace algorithm with an improved stabilization diagram method, Shock Vib. 2016 (2016).